Structural determinants of IGHV1-69 public antibodies conferring resilience to SARS-CoV-2 antigenic escape

Chuanying Niu[1,2,11], Xiaohan Huang[3,11], Qihong Yan[3,11], Banghui Liu[2,4,11], Xijie Gao[5,11], Yidong Song[6,11], Jingjing Wang[2], Longyu Wang[7,8], Zimu Li[7,8], Huiran Zheng[3], Ping He[7], Xiaodong Huang[7,8], Hang Yuan[2], Binqian Zou[2,8], Yuedong Yang[6], Fandi Wu[9], Yicheng Yao[10], Gul Habib[2], Xinwen Chen[7], Ling Chen[7,*], Jun He[2,*], Jianhua Yao[9,*], Jincun Zhao[3,*], Xiaoli Xiong[2,*]

[1]Division of Life Sciences and Medicine, University of Science and Technology of China, Hefei 230026, China.
[2]State Key Laboratory of Respiratory Disease, Guangdong Provincial Key Laboratory of Stem Cell and Regenerative Medicine, Guangdong-Hong Kong Joint Laboratory for Stem Cell and Regenerative Medicine, Guangzhou Institutes of Biomedicine and Health, Chinese Academy of Sciences, Guangzhou 510530, China.
[3]State Key Laboratory of Respiratory Disease, National Clinical Research Center for Respiratory Disease, Guangzhou Institute of Respiratory Health, the First Affiliated Hospital of Guangzhou Medical University, Guangzhou, China.
[4]Institute of Urban Agriculture, Chinese Academy of Agricultural Sciences, Chengdu 610213, China.
[5]Key Laboratory of Biological Targeting Diagnosis, Therapy and Rehabilitation of Guangdong Higher Education Institutes, The Fifth Affiliated Hospital of Guangzhou Medical University, Guangzhou 510799, China
[6]School of Computer Science and Engineering, Sun Yat-sen University, Guangzhou, Guangdong, China.
[7]Guangzhou National Laboratory, Guangzhou 510005, China.
[8]Guangzhou Medical University, Guangzhou, 511436, China.
[9]Tencent, AI for Life Sciences Lab, Shenzhen, China.
[10]School of Life Sciences, Sun Yat-sen University, Guangzhou, China.
[11]These authors contributed equally to this work.
*Corresponding author. Email: chen_ling@gibh.ac.cn (L.C.); he_jun@gibh.ac.cn (J.H.); jianhua.yao@gmail.com (J.Y.); zhaojincun@gird.cn (J.Z.); xiong_xiaoli@gibh.ac.cn (X.X.)

Abstract

R1-32-like public antibodies, characterized by shared IGHV1-69/IGLV1-40 usage, are elicited in more than 50% of individuals with COVID-19 and have been implicated in driving recurrent mutations at $L452_{SARS2}$ and $F490_{SARS2}$ within their convergent epitope in the SARS-CoV-2 spike receptor-binding domain. These mutations effectively mediate escape from non-affinity-matured R1-32-like antibodies with germline-like sequences. Here, we characterize four affinity-matured R1-32-like antibodies, C092, C807, BD56-104, and BD56-597, that tolerate $L452_{SARS2}$ and $F490_{SARS2}$ mutations. We show that this tolerance arises from residues introduced by somatic hypermutation at convergent positions across multiple CDR loops and surrounding regions, thereby creating additional contacts that reinforce epitope binding. An unusual $N354_{SARS2}$ glycosylation site, which emerged in BA.2.86 and became fixed in its descendants, is linked to escape from affinity-matured R1-32-like antibodies, implying ongoing selection by this public antibody class. Using an AI model trained on integrated structural, neutralization, and binding data, we further identified ZL525, an ultrapotent R1-32-like antibody with pan-SARS-CoV-2 variant activity, including against the highly evasive KP.3 variant carrying the $N354_{SARS2}$ glycosylation, and broad sarbecovirus cross-reactivity extending to SARS-CoV-1. Together, these findings show how affinity maturation enables public antibodies to adapt to viral antigenic drift, reveal their role in shaping SARS-CoV-2 antigenic evolution, and demonstrate the potential of AI-empowered strategies for discovering broadly neutralizing antibodies.

54 **Introduction**

55 The ongoing evolution of SARS-CoV-2, driven by immune pressure established from natural
56 infections and vaccinations, has led to extensive amino acid substitutions in the spike (S)
57 protein, the major viral surface glycoprotein and principal target of neutralizing antibodies [1-3].
58 Several key residues in the receptor-binding domain (RBD), such as $K417_{SARS2}$, $L452_{SARS2}$,
59 $E484_{SARS2}$, $F490_{SARS2}$, and $N501_{SARS2}$, have become recurrent mutation hotspots across
60 variants, enhancing immune evasion and viral fitness [1,4-8].
61
62 Based on their epitope locations, specifically whether they compete with ACE2 binding or
63 require the RBD to adopt an 'up' conformation, SARS-CoV-2 RBD-targeting antibodies have
64 been broadly classified into four epitope classes [9]. In addition, many RBD-targeting
65 antibodies isolated early in the pandemic exhibit germline-like sequences with low levels of
66 somatic hypermutation [10-12]. Some of these antibodies can be further grouped into distinct
67 public (population) antibody classes, defined by convergent epitope recognition and shared
68 genetic origins [13-15]. Such population-level responses are thought to impose strong selective
69 pressure on the virus and provide valuable insights into SARS-CoV-2 antigenic drift [16-18].
70
71 For example, many IGHV3-53/3-66-encoded public antibodies, which target the ACE2-
72 binding site and are classified as epitope class 1, were effectively abrogated by the $K417_{SARS2}$
73 mutation [9,19,20]. Many IGHV1-2-encoded public antibodies, which recognize RBD in both 'up'
74 and 'down' conformations and are classified as epitope class 2, are strongly evaded by
75 $E484_{SARS2}$ substitutions [21,22]. Notably, we identified a public antibody class defined by the use
76 of the IGLV6-57 light chain gene, which pairs with heavy chains of diverse genetic origins [14].
77 These antibodies target a class 4 epitope relatively conserved among sarbecoviruses,
78 encompassing RBD residues $S371\text{-}S373\text{-}S375_{SARS2}$. Strikingly, we show that the featured
79 Omicron $S371L/F\text{-}S373P\text{-}S375F_{SARS2}$ mutations within this epitope mediate the escape of
80 many IGLV6-57-class public antibodies [14]. Other public antibody classes, including IGHV1-
81 58/IGKV3-20 and IGHV2-5/IGLV2-14, display some breadth but remain variably
82 susceptible to escape by mutations at $F486_{SARS2}$ and positions $444\text{-}445_{SARS2}$, respectively [23-
83 26].
84
85 We have also previously identified a class of R1-32-like public antibodies elicited in more
86 than 50% of COVID-19 convalescents early in the pandemic. These antibodies are
87 characterized by shared usage of the IGHV1-69/IGLV1-40 gene pairing and rely on the
88 unique features of the IGHV1-69 gene, whose germline-encoded hydrophobic HCDR2
89 residues bind the hydrophobic RBD residues $L452_{SARS2}$ and $F490_{SARS2}$. This specific
90 interaction renders them vulnerable to mutations at L452 and F490. [16,27]. These residues have
91 since emerged as mutation hot-spots for viral escape [1,16,27]. While the Delta variant harbored
92 the $L452R_{SARS2}$ mutation, subsequent Omicron subvariants acquired $L452R/Q/M_{SARS2}$ or

93 F490S$_{SARS2}$ mutations across multiple lineages (e.g., BA.4/5, BF.7, BQ.1.1, XBB, EG.5),
94 reflecting sustained immune pressure at these positions [28-30].
95
96 Intriguingly, we found that several members of the R1-32-like public antibody class,
97 including C092, C807, BD56-104, and BD56-597, retain robust binding to S-proteins of viral
98 variants carrying mutations at positions 452$_{SARS2}$ and 490$_{SARS2}$. The mechanism by which
99 these antibodies maintain cross-variant reactivity despite substitutions at key contact residues
100 has remained unclear. In this study, we elucidate the structural and biochemical basis for their
101 mutation tolerance. We show that somatic hypermutation introduced residues, following
102 convergent patterns, confer resilience to antigenic epitope changes, including those located at
103 L452$_{SARS2}$ and F490$_{SARS2}$, and resulting in broadened reactivity not only to SARS-CoV-2
104 variants but also to other SARS-related coronaviruses. Using our structural-functional
105 relationship data, we trained an AI-based antibody discovery model [31], which led to the
106 identification of ZL525, an elite R1-32-like antibody with ultrapotent, pan-variant
107 neutralizing activity, capable of neutralizing the latest variants carrying a highly unusual
108 epitope glycan mutation and extending cross-reactivity to SARS-CoV-1. Our findings
109 illuminate the adaptability of public antibodies in response to the ongoing antigenic drift of
110 SARS-CoV-2 and highlight the power of AI-driven approaches to identify broadly-
111 neutralizing antibodies.
112

113 **Results**

114 **Identification of R1-32-like public antibodies that tolerate spike mutations**

115 We have previously defined IGHV1-69 encoded R1-32-like public antibodies as those that
116 either exhibit a minimum of 80% amino acid similarity to R1-32 or FC08 in the HCDR3
117 region or contain a GYSGYG/D motif in HCDR3 [16,27]. In our previous study, we identified
118 and characterized 10 R1-32-like antibodies isolated from ancestral (or wildtype, WT) SARS-
119 CoV-2 convalescents or vaccinees [27,32-35]. Notably, among these, C092 and C807 showed no
120 obvious reduction in binding to SARS-CoV-2 RBD variants with L452 or F490 mutations,
121 including Delta (L452R$_{SARS2}$), Kappa (L452R$_{SARS2}$), and Lambda (L452Q$_{SARS2}$+F490S$_{SARS2}$)
122 RBDs [27]. We further identified BD56-104 and BD56-597 as mutation-resistant R1-32-like
123 public antibodies that effectively neutralize Omicron subvariants BA.2.12.1 (L452Q$_{SARS2}$),
124 BA.2.13 (L452M$_{SARS2}$), and BA.4/5 (L452R$_{SARS2}$), through the analysis of published
125 sequence and neutralization data [28] (**Fig. S1a**). Notably, both BD56-104 and BD56-597 were
126 isolated from convalescents with Omicron BA.1 breakthrough infections [28]. In contrast to R1-
127 32, which has minimal somatic hypermutation (SHM), the 4 mutation-resistant antibodies,
128 C092, C807, BD56-104, and BD56-597, carry 6-15 SHMs in their heavy chains and 3-4
129 SHMs in their light chains, indicative of substantial affinity maturation (**Fig.1a and b**).
130

131 To further characterize these R1-32-like public antibodies, we performed antigen binding
132 assays for C092, C807, BD56-104, and BD56-597 against a more comprehensive and
133 updated panel of SARS-CoV-2 RBDs, which we classified into 4 categories: 1) RBDs with
134 single amino acid substitutions at key residues ($K417_{SARS2}$, $E484_{SARS2}$, $T478_{SARS2}$, $L452_{SARS2}$,
135 $F490_{SARS2}$); 2) RBDs from early VOC/VOI variants (Alpha to Lambda); 3) RBDs from early
136 Omicron variants (BA.1 to BA.4/5); and 4) RBDs from later-emerging Omicron subvariants,
137 including BQ, XBB, and EG variants. Within each category, mutants containing $L452_{SARS2}$
138 and $F490_{SARS2}$ mutations were further grouped together **(Fig. 1c and Fig. S1b-e)**.
139
140 The results showed that C092, C807, BD56-104, and BD56-597 retained high-affinity
141 binding (K_D < 1.2 nM) to SARS-CoV-2 RBDs carrying $L452_{SARS2}$ and $F490_{SARS2}$ single
142 mutations. In contrast, the germline-like R1-32 exhibited substantially reduced binding to
143 these mutant RBDs (K_D = 11.8-54.2 nM) **(Fig. 1c and Fig. S1b-e)**. Substitutions at
144 $K417_{SARS2}$, $E484_{SARS2}$, and $T478_{SARS2}$, commonly associated with the escape of epitope class
145 1 and class 2 antibodies [9,20,21], had minimal impact on the binding of C092, C807, BD56-104,
146 and BD56-597 **(Fig. 1c and Fig. S1b-e)**, consistent with these residues being located at the
147 periphery or outside of the epitope recognized by the R1-32 class of public antibodies.
148
149 C092, C807, BD56-104, and BD56-597 maintained very high affinities (K_D < 0.3 nM)
150 towards RBDs of variants carrying no mutations at 452_{SARS2} or 490_{SARS2}, including Alpha
151 (B.1.1.7), Beta (B.1.351), Gamma (P.1), and multiple Omicron sublineages (BA.1, BA.1.1,
152 BA.2, BA.3, BA.2.75, and BA.2.75.2). Consistent with their mutation tolerance, C092, C807,
153 BD56-104, and BD56-597 also maintained high affinities (K_D < 2.1 nM) towards RBDs
154 harboring $L452_{SARS2}$ substitutions, including Kappa (B.1.617.1), Delta (B.1.617.2), Omicron
155 BA.2.11, BA.2.12.1, BA.2.13, BA.4/5, BF.7, and BQ.1.1. For comparison, germline-like R1-
156 32 exhibited substantially reduced binding to these mutants (K_D > 55 nM).
157
158 Notably, C092, C807, BD56-104, and BD56-597 maintained high affinities (K_D < 4.5 nM)
159 towards RBDs of the later emerged XBB lineages (XBB, XBB.1.5), and EG.5 lineages
160 (EG.5, EG.5.1), despite the presence of $F490S_{SARS2}$ mutations in these variants. All four
161 antibodies exhibited the weakest binding to the Lambda (C.37) RBD carrying both the
162 $L452_{SARS2}$ and $F490_{SARS2}$ mutations, although their K_D values are still below 6.8 nM **(Fig. 1c**
163 **and Fig. S1b-e)**. For comparison, the germline-like R1-32 binds Lambda RBD with a K_D of ~
164 1000 nM, representing a reduction of ~1000-fold.
165
166 These RBD binding results confirm that BD56-104 and BD56-597, like C092 and C807, are
167 tolerant to diverse variants carrying $L452_{SARS2}$ and $F490_{SARS2}$. Among them, we found that
168 C092 and BD56-597 consistently exhibited more robust binding across RBD variants
169 compared to C807 and BD56-104. C807 showed moderately but noticeably reduced binding
170 to RBDs harboring $L452_{SARS2}$ mutations, such as those in Kappa, Delta, Lambda, Omicron

171 BA.4/5, BF.7, and BQ.1.1, characterized by accelerated dissociation kinetics (**Fig. S1c**).
172 BD56-104 also showed moderate but noticeable sensitivity to $F490_{SARS2}$ substitutions,
173 displaying accelerated dissociation from RBDs of Lambda, XBB lineages (XBB, XBB.1.5),
174 and EG.5 lineages (EG.5, EG.5.1) that carry this mutation (**Fig. S1d**).
175

176 Mutation-tolerant antibodies retain potent neutralization against diverse 177 SARS-CoV-2 variants

178 Neutralization activities of C092, C807, BD56-104, and BD56-597 were evaluated using
179 VSV-based pseudovirus neutralization assays [36] against eight variants of SARS-CoV-2: the
180 ancestral SARS-CoV-2 strain (WT), Delta (B.1.617.2), Lambda (C.37), Omicron BA.1
181 (B.1.1.529), BA.2, BA.4/5, BA. 2.75.2, BQ.1.1, and EG.5. The results showed that all four
182 antibodies neutralized all tested variants, with IC_{50} values ranging from 0.022 to 7.557 μg/mL
183 **(Fig. 1d and e)**. However, compared with the WT, obvious reductions in neutralization
184 activity were observed for Delta ($L452R_{SARS2}$), Lambda ($L452Q_{SARS2}$+$F490S_{SARS2}$), BA.4/5
185 ($L452R_{SARS2}$), BQ.1.1 ($L452R_{SARS2}$), and EG.5 ($F490S_{SARS2}$) variants containing $L452_{SARS2}$,
186 $F490_{SARS2}$, or both mutations. By contrast, germline-like R1-32 lost neutralization (IC_{50} >10
187 μg/mL) against Delta, Lambda, BA.4/5, BQ.1.1, and EG.5 pseudoviruses.
188
189 Consistent with pseudovirus neutralization assays, C092, C807, BD56-104, and BD56-597
190 demonstrated potent neutralization (most IC_{50} <10 μg/mL) against authentic SARS-CoV-2
191 variants, including Delta ($L452R_{SARS2}$), BA.5 ($L452R_{SARS2}$), BQ.1($L452R_{SARS2}$),
192 XBB.1($F490S_{SARS2}$), and EG.5 ($F490S_{SARS2}$), while R1-32 showed no detectable
193 neutralization (IC_{50} >100 μg/mL) against these variants **(Fig. 1f and g)**. However, all five
194 antibodies lost neutralizing activities against the recent circulating variant KP.3.
195 Complementing the neutralization data, C092, C807, BD56-104, and BD56-597 exhibited
196 strong, non-dissociating binding to the S-trimers of variants neutralized in the neutralization
197 assays **(Fig. S2)**. Binding affinity assays revealed moderately weakened binding with
198 Lambda ($L452Q_{SARS2}$+$F490S_{SARS2}$), BA.4/5 ($L452R_{SARS2}$), and BQ.1.1 ($L452R_{SARS2}$) S-
199 trimers relative to WT, consistent with the observed reduction in neutralization potency
200 against these variants. Altogether, our neutralization and binding data demonstrate that C092,
201 C807, BD56-104, and BD56-597 exhibit markedly enhanced breadth and mutation tolerance
202 compared to the germline-like R1-32, maintaining neutralization activity against SARS-CoV-
203 2 variants carrying $L452_{SARS2}$, $F490_{SARS2}$, or even both escape mutations, with minimal to
204 modest reductions in potency.
205

206 **Binding of R1-32-like antibodies disassembles S-trimer without blocking**
207 **ACE2 binding**

208 To elucidate how C092, C807, BD56-104, and BD56-597 tolerate mutations to cross-
209 neutralize SARS-CoV-2 variants, we prepared cryo-electron microscopy (cryo-EM) samples
210 using stoichiometric mixtures of Fab, ACE2, and BA.4/5 S-trimer (Fab:ACE2:S-protomer =
211 1:1:1). Cryo-EM structures of C092, C807, BD56-104, and BD56-597 Fabs bound to BA.4/5
212 S-trimer in complex with ACE2 were determined (**Fig. 2a and Figs. S5-9**).
213
214 For the C092 Fab:ACE2:S-trimer sample, each S-trimer was found to adopt either 2 or 3
215 RBD "up" conformations, allowing simultaneous binding of either 2 or 3 Fab and ACE2
216 molecules. All other structures showed S-trimers with all three RBDs in the "up" position,
217 with each RBD concurrently engaging both ACE2 and Fab **(Figs. S5-8)**. Consistent with
218 previous conclusions [27], these S-trimer structures confirm that R1-32-like public antibodies
219 do not interfere with ACE2 binding, in agreement with results from the antibody-ACE2
220 competition assays **(Fig. S3)**. In addition to ligand bound S-trimer structures, we also
221 observed isolated S1 domains bound to both Fab and ACE2, suggesting that a portion of S-
222 trimers disassembles upon simultaneous antibody and ACE2 binding. **(Figs. S5-8)**. Based on
223 these disassembled particles, Structures of C092, C807, BD56-104, and BD56-597 bound to
224 ACE2 bound S1 domain were determined to high-resolutions (2.58 - 2.83 Å) **(Fig. 2b and**
225 **Figs. S5-9)**. We previously concluded that R1-32 neutralizes SARS-CoV-2 by inducing
226 disassembly of S-trimers, thereby rendering them incapable of mediating membrane fusion [27].
227 Based on the imaging data, we infer that C092, C807, BD56-104, and BD56-597 similarly
228 retain the ability to induce disassembly of S-trimers from variant viruses.
229

230 **R1-32-like antibodies impair spike fusogenic conformational change**

231 To further confirm the neutralization mechanism, we conducted ligand-induced
232 conformational change assays. The results showed that, like the WT, BA.4/5 S-trimers can be
233 triggered by ACE2-Fc or YB9-258 [37], an epitope class 1 antibody that can mimic ACE2
234 function, to undergo the fusogenic conformational change, generating the proteinase K-
235 resistant S2 fusion core **(Fig. S4a and c)**. ACE2-Fc retains the ability to trigger the EG.5.1 S-
236 trimer, whereas YB9-258 loses this ability, likely due to epitope mutations in EG.5.1 that
237 disrupt YB9-258 binding **(Fig. S4e)**. In line with our previous findings, S-trimers (WT,
238 BA.4/5, and EG.5.1) pre-incubated with R1-32 and the four antibodies (C092, C807, BD56-
239 104, and BD56-597) were unable to undergo structural transition into a post-fusion
240 conformation **(Fig. S4a, c, and e).**
241
242 Further, assay results also showed that WT, BA.4/5, and EG.5 S-trimers pre-incubated with
243 the four R1-32-like antibodies (C092, C807, BD56-104, or BD56-597) were unable to
244 undergo the fusogenic conformational change upon subsequent addition of ACE2. **(Fig. S4b,**

245 **d, and f)**. In contrast, although R1-32 efficiently impairs the fusogenic conformational
246 change of the WT S-trimer, it only partially inhibits this transition in the BA.4/5 and EG.5 S-
247 trimers **(Fig. S4b, d, and f)**, likely due to the presence of $L452_{SARS2}$ or $F490_{SARS2}$ mutations
248 in these variants. This reduced inhibition correlates with R1-32's diminished neutralization
249 activity against the corresponding variants.
250
251 Together with our cryo-EM data showing disassembled S-trimers, the results from ligand-
252 induced conformational change assays confirm that the four identified R1-32-like antibodies
253 retain the ability to inhibit ACE2-induced fusogenic conformational changes of S-trimers
254 from variant viruses, likely by destabilizing or disassembling S-trimers, as previously
255 proposed for R1-32 against the WT virus [27]. The results are further consistent with
256 neutralization assays demonstrating superior resilience of C092, C807, BD56-104, and
257 BD56-597 against $L452_{SARS2}$- and $F490_{SARS2}$-bearing variants compared to R1-32.
258

259 Broadly neutralizing public antibodies maintain binding to the mutated 260 convergent epitope

261 The newly determined C092, C807, BD56-104, and BD56-597 complex structures were
262 aligned to our previously reported R1-32 complex structure (PDB: 7YDI), using the RBD as
263 the reference **(Fig. 2c)**. Based on this alignment, the root mean square deviations (RMSDs) of
264 the Fab variable regions were calculated as follows: C092 (1.5 Å), C807 (1.8 Å), BD56-104
265 (1.7 Å), and BD56-597 (1.5 Å). The low RMSD values indicate that these antibodies adopt
266 binding modes and recognize epitopes nearly identical to those of R1-32 **(Fig. 2c, left panel)**.
267
268 Antibody interface analysis reveals that all four R1-32-like antibodies engage the RBD
269 through both their heavy and light chains, with a predominant contribution from the heavy
270 chains: C092 binds an epitope area of 1,350 $Å^2$ (HC: 903 $Å^2$, LC: 447 $Å^2$); C807 binds an
271 epitope area of 1,193 $Å^2$ (HC: 820 $Å^2$, LC: 373 $Å^2$); BD56-104 binds an epitope area of 1,148
272 $Å^2$ (HC: 765 $Å^2$, LC: 383 $Å^2$); and finally BD56-597 binds an epitope area of 1,290 $Å^2$ (HC:
273 937 $Å^2$, LC: 353 $Å^2$). For comparison, the germline-like R1-32 binds an epitope area of
274 1,214 $Å^2$ (HC: 813 $Å^2$, LC: 401 $Å^2$).
275
276 All four R1-32-like antibodies utilize their characteristic IGHV1-69 HCDR2, featuring
277 hydrophobic residues at positions 52_H, 54_H, and 55_H (subscripts denote heavy (H) or light (L)
278 chain), to engage the hydrophobic RBD residues $F490_{SARS2}$ and $L492_{SARS2}$ (**Fig. 3a-d, left**
279 **panels**). Notably, within the epitopes of R1-32-like antibodies in the BA.4/5 RBD, the
280 epitope substitution $L452R_{SARS2}$ is present, with the aliphatic portion of $R452_{SARS2}$ sidechain
281 contacted by the hydrophobic HCDR2 residue 55_H. HCDR3 residues 102_H, 103_H, 104_H, and
282 107_H form polar interactions with RBD residues $E465_{SARS2}$, $R466_{SARS2}$, and $I468_{SARS2}$ (**Fig.**
283 **3a-d, right panels**). Additionally, HCDR1 (**Fig. 3a-d, left panels**) and LCDR1 (**Fig. 3a-d,**

284 **middle panels**) contribute to RBD binding in all four antibodies. Notably, in C092, unlike
285 the other three antibodies, both the light chain framework region 3 (LFR3) and LCDR3
286 participate in RBD binding (**Fig. 3a, middle panel**). Also notably, in BD56-104 and BD56-
287 597, the heavy chain backbone region 3 (HFR3) participates in RBD binding (**Fig. 3c and d,**
288 **left panels**).
289
290 We previously found that somatic hypermutation (SHM)-introduced residues play a key role
291 in enhancing antigen binding and conferring mutation tolerance [22,37]. Compared with the
292 germline antibody R1-32 (**Fig. S9e**), all four antibodies harbor SHM-introduced residues in
293 HCDR1 and LCDR1 (**Fig. 3a-d**). In C092, SHM-introduced residues are also present in
294 LFR3 and LCDR3 (**Fig. 3a**). In BD56-104 and BD56-597, SHM-introduced residues are also
295 found in heavy chain framework region 3 (HFR3) (**Fig. 3c and d**). Many of these residues
296 form additional contacts with the RBD, likely contributing to enhanced antigen binding (see
297 below).
298

299 Convergent somatic hypermutations confer enhanced binding and 300 mutation tolerance

301 C092, C807, BD56-104, and BD56-597 likely resist epitope mutations by having undergone
302 affinity maturation through somatic hypermutation. To investigate the affinity maturation
303 pathway underlying their mutation tolerance, we curated ninety-eight R1-32-like antibodies
304 from sequences reported by Cao *et al.*[28] and analyzed the correlation between SHM patterns
305 and neutralization activity (IC_{50} values). We examined whether specific mutations are
306 enriched in the R1-32-like antibodies isolated from individuals with different exposure
307 histories **(Fig. S10)**, as well as antibodies escaped by or tolerant to BQ.1.1 ($L452R_{SARS2}$) and
308 XBB ($F490S_{SARS2}$) **(Fig. 4a)**. We found several SHMs are highly enriched in R1-32-like
309 antibodies that tolerant to BQ.1.1 and XBB, such as $A33P/S_H$, $S35T_H$, and $N59D_H$ on the
310 heavy chain and $S26N_L$, $G52A/V_L$, and $S54N/T_L$ on the light chain **(Fig. 4a)**. In addition,
311 these SHMs were enriched in R1-32-like antibodies isolated from patients with breakthrough
312 infections (**Fig. S10**). Several of these SHM-enriched sites are also directly involved in
313 epitope binding in C092, C807, BD56-104, and BD56-597 (**Fig. 3**).
314
315 In the C092:RBD complex, SHM introduced HCDR1 residues $N31_H$ and $H32_H$ form a
316 hydrogen bond and a salt bridge with RBD residues $T470_{SARS2}$ and $E471_{SARS2}$, respectively
317 (**Fig. 3a, left panel**). SHM introduced HCDR1 residue $F33_H$ contacts RBD residues
318 $I468_{SARS2}$ and $Y351_{SARS2}$, as well as HCDR2 residue $I52_H$, thereby reinforcing the
319 hydrophobic interactions involving $I52_H$, $I54_H$, and $L55_H$ of HCDR2 and RBD residues
320 $F490_{SARS2}$ and $L492_{SARS2}$ (**Fig. 3a, left and right panels**). Additionally, SHM-introduced
321 residues in the light chain further enhance antigen binding: $N26_L$ of LCDR1 and $D70_L$ of
322 LFR3 form hydrogen bonds and salt bridges with $R357_{SARS2}$, while $D99_L$ of LCDR3 forms

323 salt bridges with R346$_{SARS2}$ **(Fig. 3a, middle panel)**. To confirm the function of the SHM-
324 introduced residues, we reverted them to their germline sequences and evaluated antigen
325 binding by the revertants. Reverting C092 HCDR1 to germline reduced binding to L452R,
326 Kappa (L452R$_{SARS2}$), Delta (L452R$_{SARS2}$), Lambda (L452Q$_{SARS2}$+F490S$_{SARS2}$), and BA.4/5
327 (L452R$_{SARS2}$) RBDs by ~ 10-fold (**Fig. 4b and Fig. S11a**). Likewise, reverting the light chain
328 SHM-introduced residues (N26S$_L$, D70G$_L$, and D99G$_L$) to germline reduced binding to the
329 same set of RBDs by ~10-100-fold.
330
331 In the C807:RBD complex, SHM-introduced HCDR1 residue I33$_H$ contacts RBD residues
332 I468$_{SARS2}$ and Y351$_{SARS2}$, as well as I52$_H$ of HCDR2, via hydrophobic interactions **(Fig. 3b,**
333 **left and right panels)**. Therefore, I33$_H$ of C807, like F33$_H$ in C092, enhances the
334 hydrophobic interactions mediated by HCDR2. Reverting HCDR1 of C807 into the germline
335 sequence reduced binding of RBDs with 452$_{SARS2}$ and 490$_{SARS2}$ mutations **(Fig. 4c and Fig.**
336 **S11b)**.
337
338 In the BD56-104:RBD complex, SHM-introduced HFR3 residue D59$_H$ forms salt bridges
339 with the mutated RBD residue R452$_{SARS2}$, while SHM-introduced HFR3 residue E62$_H$ forms
340 salt bridges with R346$_{SARS2}$ **(Fig. 3c, left panel)**. Germline reversion of HFR3 residues
341 (D59N$_H$ and E62Q$_H$) reduced binding to RBDs carrying 452$_{SARS2}$ and 490$_{SARS2}$ mutations. In
342 particular, the combined BD56-104 HFR3 revertant (D59N$_H$/E62Q$_H$) showed an ~100-fold
343 reduction in binding to the BA.4/5 RBD harboring the L452R$_{SARS2}$ mutation **(Fig. 4d and**
344 **Fig. S11c)**.
345
346 In the BD56-597:RBD complex, similar to C092 and C807, SHM-introduced HCDR1 residue
347 P33$_H$ provides extra hydrophobic interactions to enhance antigen binding **(Fig. 3d, left and**
348 **right panels)**. Further, similar to BD56-104, SHM-introduced HFR3 residue D59$_H$ forms salt
349 bridges with the mutated RBD residue R452$_{SARS2}$ **(Fig. 3d, left panel)**. Notably, SHM-
350 introduced LCDR1 residue D26$_L$ interacts with R357$_{SARS2}$ via salt bridges **(Fig. 3d, middle**
351 **panel)**. Germline reversion of HCDR1, HFR3 (D59N$_H$), and LCDR1 (D26S$_L$) reduced
352 binding to the RBDs carrying 452$_{SARS2}$ and 490$_{SARS2}$ mutations. Notably, towards the Lambda
353 RBD, carrying both L452Q$_{SARS2}$+F490S$_{SARS2}$ mutations, a 10-fold reduction in binding was
354 observed **(Fig. 4e and Fig. S11d)**.
355

356 ## HCDR3 synergizes with somatic mutations to confer mutation tolerance

357 In addition to the extra interactions mediated by SHM-introduced residues, HCDR3 also
358 contributes to enhanced antigen binding in C092, C807, and BD56-597. Antigen-binding
359 assays showed that replacing the HCDR3s of C092, C807, or BD56-597 with that of R1-32
360 (97$_H$-ARENGYSGYGAA**A**NFDL-113$_H$, with A109$_H$ underlined in bold) markedly reduced
361 binding to the tested RBDs, with C807 being the most affected (**Fig. 4b-e and Fig. S11**). In

contrast, HCDR3 substitution in BD56-104 had a comparatively minor impact on binding. Structural data revealed that the HCDR3s of C092, C807, and BD56-597 all contain a shared $Y109_H$, which forms hydrogen bonds and hydrophobic interactions with RBD residues $Y351_{SARS2}$ and $I468_{SARS2}$ (**Fig. 3a, b, and d, right panels**). Substituting $Y109_H$ with the alanine present in R1-32 also notably impaired antigen binding in these three antibodies. Moreover, combining HCDR1 germline reversion with the HCDR3 $Y109A_H$ substitution in C092, C807, and BD56-597 produced an additive reduction in binding (**Fig. 4b-e and Fig. S11**), indicating that distinct antigen-contact regions act synergistically to achieve high-affinity binding.

Artificial affinity maturation of R1-32 validates SHM-introduced residues in enhancing mutation tolerance

Our structural and antigen-binding data confirmed seven residues enriched with mutations and associated with enhanced antigen binding, $A33F_H$, $N59D_H$, $Q62E_H$, and $A109Y_H$ in the heavy chain, and $S26D_L$, $G70D_L$, and $G99D_L$ in the light chain. We introduced these residues into R1-32 to generate an antibody called termed "R1-32-AAM" (R1-32-artificial-affinity-matured). Notably, these SHM-introduced residues not only mediate additional RBD interactions in C092, C807, BD56-104, and BD56-597, but most of them are also enriched in R1-32-like antibodies that retain tolerance to BQ.1.1 and XBB (**Fig. 4a**).

Binding assays showed that R1-32-AAM exhibits markedly enhanced antigen-binding activity compared with R1-32. Relative to R1-32, R1-32-AAM bound to RBDs bearing L452 mutation, including $L452R_{SARS2}$, Kappa ($L452R_{SARS2}$), Delta ($L452R_{SARS2}$), Lambda ($L452Q_{SARS2}$+$F490S_{SARS2}$), BA.4/5 ($L452R_{SARS2}$), BF.7 ($L452R_{SARS2}$), and BQ.1.1 ($L452R_{SARS2}$) with faster association, slower dissociation, and resulting in ~100-fold enhanced affinity (**Fig. 4f**). It also displayed enhanced binding to RBDs carrying $F490S_{SARS2}$ or $F490W_{SARS2}$, and XBB variant ($F490S_{SARS2}$), with ~10-100-fold higher affinity than R1-32. Consistent with these binding data, R1-32-AAM neutralized authentic Delta ($L452R_{SARS2}$), BA.5 ($L452R_{SARS2}$), XBB.1 ($F490S_{SARS2}$), and EG.5 ($F490S_{SARS2}$) viruses (**Figs. 1f and g and 4g and h**), confirming that SHM-introduced residues enriched among R1-32-like antibodies confer tolerance to $L452_{SARS2}$ and $F490_{SARS2}$ substitutions. Together with structural differences to R1-32 (**Fig. S9e**), these findings indicate that the breadth of C092, C807, BD56-104, and BD56-597 is largely attributable to affinity-maturation-introduced residues, particularly within and around the CDRs, which mediate additional antigen interactions.

398 **Affinity maturation broadens the activity of R1-32-like antibodies toward**
399 **SARSr-CoV RBDs**

400 We further explored potential cross-reactivities of C092, C807, BD56-104, and BD56-597
401 toward SARSr-CoV RBDs using antigen-binding assays **(Fig. 5a and Fig. S12)**, testing
402 representative type-1 to type-3 RBDs as previously defined by the extent of deletions within
403 the receptor-binding motif (RBM) [38]. All four antibodies bound the "type-1" RBDs of
404 Pangolin-GD-2019, Bat-RaTG13, Pangolin-GX-2017, Laos-20-52, Laos-20-236, and Bat-
405 RsSHC014 with affinities ranging from 0.016 to 48 nM. Notably, C092, C807, and BD56-
406 597 cross-reacted to WIV1 RBD, whereas BD56-104 did not. Only C807 and BD56-597
407 bound the SARS-CoV-1 RBD, albeit with much compromised affinities (K_D < 341 nM) **(Fig.**
408 **5a)**. Remarkably, all four antibodies also bound the "type-2" BtKY72 RBD, despite its RBM
409 sequence differing notably from the "type-1" SARS-CoV-2 RBD. Moreover, they retained
410 binding to the "type-3" RBDs of GX2013, HeB2013, and RmYN02, which contain
411 substantial loop deletions within the RBM region **(Fig. 5a)**. Among them, C092 and C807
412 exhibited tighter binding affinities than BD56-104 and BD56-597, demonstrating broader
413 cross-reactivity towards SARSr-CoV RBDs. In contrast, R1-32 showed much weaker binding
414 to the RBDs of Bat-RaTG13, Pangolin-GX-2017, and Bat-RsSHC014 (4.76-297 nM) than
415 C092, C807, BD56-104, BD56-597, and failed to bind the RBDs of Bat-WIV1, SARS-CoV-
416 1, BtKY72, GX2013, HeB2013, and RmYN02 **(Fig. 5a)**, indicating that affinity maturation
417 confers broader SARSr-CoVs binding to R1-32-like antibodies.
418
419 We have established that C092, C807, BD56-104, and BD56-597 can well tolerate and
420 maintain almost uncompromised neutralization towards variants carrying 1 mutation at RBD
421 residues 452_{SARS2} or 346_{SARS2}, including Delta ($L452R_{SARS2}$), BA.5 ($L452R_{SARS2}$), and
422 BA.2.75.2 ($R346T_{SARS2}$). Neutralization was somewhat reduced towards variants with 2
423 mutations within the RBD epitope, including Lambda ($L452Q_{SARS2}$+$F490S_{SARS2}$), BQ.1.1
424 ($R346T_{SARS2}$+$L452R_{SARS2}$), XBB.1 ($R346T_{SARS2}$+$F490S_{SARS2}$), and EG.5
425 ($R346T_{SARS2}$+$F490S_{SARS2}$) **(Fig. 1c-g)**. We noted that all four R1-32-like antibodies exhibited
426 markedly impaired binding to the SARS-CoV-1 RBD. Within the R1-32-like antibody
427 epitope, SARS-CoV-1 and SARS-CoV-2 differ at $L452_{SARS2}$, $F490_{SARS2}$, $R346_{SARS2}$,
428 $R357_{SARS2}$, and $T470_{SARS2}$. To assess the mutation tolerance of the four R1-32-like antibodies
429 **(Fig. S13)**, we introduced $R346T_{SARS2}$, $R357T_{SARS2}$, and $T470N_{SARS2}$ mutations into the
430 Lambda ($L452Q_{SARS2}$+$F490S_{SARS2}$) RBD, towards which C092, C807, BD56-104, and BD56-
431 597 already exhibited 9.5-178-fold reduction in binding affinity (**Fig. 1c)**. Introduction each
432 single mutation into the Lambda RBD further reduced binding affinity by 4.6-59-fold (**Fig.**
433 **S13b)**. We previously found that antibody neutralization is more impacted by reduced
434 antigen association than by accelerated antigen dissociation, as the latter can be compensated
435 by avidity [22]. Notably, these mutated RBDs impacted both antibody association and
436 dissociation, with association rates (k_{on}) reduced by 2.6-12-fold (**Fig. S13c)**, thereby 3 epitope

437 mutations likely impact neutralization. For BD56-104, Lambda+R346T$_{SARS2}$+T470N$_{SARS2}$,
438 completely abolished binding. For C092, C807, and BD56-597, we found that only when all
439 three mutations (R346T$_{SARS2}$, R357T$_{SARS2}$, and T470N$_{SARS2}$) were introduced simultaneously
440 into the Lambda RBD did the antibodies completely lose binding **(Fig. S13b and c)**. These
441 data suggest that C092, C807, BD56-104, and BD56-597 can still maintain antigen binding,
442 withstanding 3-4 mutations in the epitope.
443
444 To further investigate cross-reactivity, the C092 Fab and D1H4 Fab [22] were incubated with
445 the GX2013 S-trimer. Cryo-EM imaging of the sample revealed S-trimer disassembly. A 3.45
446 Å resolution structure of the C092 Fab:D1H4 Fab:GX2013 S1 complex was determined from
447 disassembled S-trimer particles **(Fig. 5b and c and Fig. S14)**. The complex was aligned to
448 the C092 Fab:BA.4/5 RBD complex using the RBDs as references to compare the difference
449 of C092 binding to GX2013 and BA.4/5 RBDs. The result shows that C092 binds to the same
450 epitope area on both the GX2013 and BA.4/5 RBDs **(Fig. 5d)**. C092 binds an epitope area of
451 1,003 Å^2 on GX2013 RBD, with 675 Å^2 buried by HCDRs, and 328 Å^2 buried by LCDRs.
452 This binding interface is smaller than the C092:BA.4/5 RBD interface (1,350 Å^2), consistent
453 with weaker binding of C092 to GX2013 RBD than BA.4/5.
454
455 In the C092:GX2013 RBD complex, the HCDR2 loop contains hydrophobic residues I52$_H$,
456 I54$_H$, and L55$_H$ and interacts with residues Y438$_{GX}$ (L452$_{SARS2}$), Y463$_{GX}$ (F490$_{SARS2}$), and
457 L465$_{GX}$ (L492$_{SARS2}$) on GX2013 RBD via hydrophobic interaction. These hydrophobic
458 interactions are further strengthened by the SHM-introduced HCDR1 residue F33$_H$ via extra
459 hydrophobic contacts **(Fig. 5e, left panels)**. The HCDR3 contacts GX2013 RBD residues -
460 E451$_{GX}$ (E465$_{SARS2}$), R452$_{GX}$ (R466$_{SARS2}$), L454$_{GX}$ (I468$_{SARS2}$) and Y342$_{GX}$ (Y351$_{SARS2}$),
461 with Y102$_H$, S103$_H$, G104$_H$, S107$_H$, and Y109$_H$ via extensive hydrogen bonds **(Fig. 5e, right**
462 **panel)**. Further, SHM-introduced HCDR1 N31$_H$ and LCDR1 N26$_L$ form hydrogen bonds
463 with S456$_{GX}$ (T470$_{SARS2}$) and K348$_{GX}$ (R357$_{SARS2}$), respectively, to strengthen antigen
464 binding. **(Fig. 5e, left and middle panel)**. Therefore, we conclude that affinity maturation is
465 a key driver for broadening the reactivity of R1-32-like antibodies toward SARSr-CoV
466 RBDs, with SHM-introduced residues mediating additional antibody-antigen interactions.
467

468 AI-guided discovery of an ultrapotent broadly neutralizing antibody
469 tolerant to glycan-mediated immune escape

470 Structure-guided artificial affinity maturation of R1-32 markedly enhanced its tolerance to
471 viral escape mutations, whereas natural affinity maturation broadened the activity of this
472 antibody class against sarbecoviruses with considerably diverged RBD epitopes, highlighting
473 their potential for further expansion of breadth against emerging SARS-CoV-2 variants.
474 Although C092, C807, BD56-104, and BD56-597 retained neutralizing activity against
475 variants generally with 2 epitope mutations, including Lambda (L452Q$_{SARS2}$+F490S$_{SARS2}$),

476 BQ.1.1 (R346T$_{SARS2}$+L452R$_{SARS2}$), XBB.1 (R346T$_{SARS2}$+F490S$_{SARS2}$), and EG.5
477 (R346T$_{SARS2}$+F490S$_{SARS2}$), the emerging KP.3 variant completely escaped their
478 neutralization (**Fig. 1f and g**).
479
480 To discover antibodies with broader reactivity, we employed an AI-driven approach to
481 discover R1-32-like antibodies with ultrapotent activities. We developed a deep learning
482 model to predict antibody-antigen binding affinity, followed by subsequent stratified virtual
483 screening to prioritize candidates (**Fig. 6a**). We pre-trained separate RoFormer-based [39]
484 language models for antibody heavy and light chains and antigen, using a masked amino acid
485 prediction task. Antigen representations were generated using the evolutionary-scale model
486 ESM2 [40]. Embeddings from both antibody and antigen models were integrated through a
487 multilayer perceptron, followed by fine-tuning based on a consolidated antigen binding
488 affinity dataset.
489
490 The constructed affinity prediction model was used to screen 190 curated R1-32-like mAbs.
491 A lead candidate, ZL525, which derived from an individual with sequential BA.5 and XBB
492 breakthrough infections and exhibited higher predicted affinity than C092, C807, BD56-104,
493 and BD56-597 (**Fig. 6b**). Authentic virus neutralization assays showed that ZL525 effectively
494 neutralized all tested SARS-CoV-2 variants, including Beta, Delta, BA.1, BA.5, BQ.1,
495 XBB.1, EG.5, and KP.3, with IC_{50} values ranging from 0.044 to 7.193 μg/mL **(Fig. 6c and**
496 **d)**. Of note, ZL525 exhibited an excellent IC_{50} value of 0.107 μg/mL against KP.3, in
497 contrast to C092, C807, BD56-104, and BD56-597, which completely lost neutralizing
498 activity against the emerging KP.3 variant (IC_{50} > 100 μg/mL) **(Fig. 1f and g)**, underscoring
499 ZL525 as an ultrapotent broadly neutralizing antibody. Consistent with the neutralization
500 assays, ZL525 exhibited high affinities (below 0.71 nM) for the RBDs carrying L452$_{SARS2}$,
501 F490$_{SARS2}$, or both mutations, including Delta, Kappa, Lambda, BA.4/5, BQ.1.1, XBB.1.5,
502 and EG.5.1**(Fig. 6e and Fig. S16c)**. Furthermore, ZL525 maintained strong binding affinities
503 (below 1.11 nM) for newly emergent variants, including HK.3, JD.1.1, BA.2.86, JN.1, KP.2,
504 and KP.3, confirming its potential as a broadly therapeutic candidate. In addition, ZL525
505 demonstrated enhanced cross-reactivity towards sarbecoviruses, by comparison with C092,
506 C807, BD56-104, and BD56-597, binding to all tested sarbecovirus RBDs, including SARS-
507 CoV-1(**Fig. 5a**).
508
509 To understand ZL525 mutation tolerance, the LP.8.1 S-trimer was incubated with ZL525 Fab
510 and ZL58 Fab (of a IGHV3-53 antibody). S-trimers in a 3-RBD "up" conformation with each
511 RBD bound to a ZL525 Fab and a ZL58 Fab were imaged. By focused refinement, a 2.93Å
512 ZL525 Fab: ZL58 Fab:LP.8.1 RBD complex structure was determined. **(Fig. 6f and Fig.**
513 **S15)**. As expected, ZL525 recognizes the convergent epitope bound by other R1-32-like
514 antibodies. Of note, its HCDR2 contains two characteristic SHM-introduced residues A55$_H$
515 and M57$_H$ to contact the RBD hydrophobic patch W452$_{SARS2}$, F490$_{SARS2}$, and L492 $_{SARS2}$ on

516 RBD **(Fig. 6f, left panel)**. Structural superposition of the BA.4/5 RBD:C092 and LP.8.1
517 RBD:ZL525 complexes reveals a conformational perturbation in the HCDR2 loop of ZL525.
518 This conformational perturbation appears to allow HCDR2 to better contact the mutated
519 L452W$_{SARS2}$ residue **(Fig. S16a).** The above hydrophobic interactions are further enhanced
520 by SHM-introduced HCDR1 residue P33$_H$. Similar to C092, SHM-introduced residues
521 LCDR1 residue N26$_L$ and LFR3 residue D70$_L$ form hydrogen bonds and salt bridges with
522 R357, respectively, to further enhance interaction **(Fig. 6f, middle panel)**. Compared with
523 C092, C807, BD56-104, and BD56-597, ZL525 exhibits a distinctive structural feature: SHM
524 introduced residues within HCDR2 (A55$_H$ and M57$_H$) directly contact epitope. Although
525 BD56-104 and BD56-597 contain SHM-introduced residues in HCDR2 (I51V$_H$ and A58P$_H$ in
526 BD56-104, A58T$_H$ in BD56-597), these residues are not involved in epitope contact with
527 their side-chains orienting away from the epitope.
528
529 Notably, our structure reveals that the newly introduced N354$_{SARS2}$ glycosylation [41,42] maps
530 directly onto this public antibody epitope **(Fig. 6f, middle panel and Fig. S16b)**, suggesting
531 that glycan shielding may obstruct antibody recognition. To test this, we engineered
532 T356K$_{SARS2}$ mutants of BA.2.86, JN.1, KP.2, and KP.3 RBDs to eliminate the N354$_{SARS2}$
533 glycosylation. All four antibodies exhibited restored high-affinity binding to these glycan-
534 revertants, with markedly improved association rates (k_{on}) **(Fig. S16d)**, confirming that the
535 N354$_{SARS2}$ glycosylation contributes to their escape. In contrast, the AI-identified antibody
536 ZL525 exhibits greater tolerance to this glycan-mediated shielding, likely due to structural
537 adaptations introduced by somatic hypermutation. Collectively, these findings establish
538 N354$_{SARS2}$ glycan shielding as a key antigenic change driving immune evasion in emerging
539 KP.3 lineage variants, consistent with previous reports[43], and highlight ZL525 as a broadly
540 neutralizing antibody capable of overcoming this glycan-mediated escape mechanism.
541

542 ## Discussion

543 Through a series of structural and biochemical analyses, we now understand that affinity-
544 matured R1-32-like public antibodies, including C092 and C807 [27] as well as BD56-104 and
545 BD56-597 [28], retain binding to their convergent epitope, tolerating the L452$_{SARS2}$ and
546 F490$_{SARS2}$ mutations through additional interactions mediated by SHM-introduced residues.
547 We further find that affinity-matured C092, C807, BD56-104, and BD56-597 maintain
548 neutralizing activity against viruses carrying at least two epitope mutations, exemplified by
549 the Lambda variant (L452Q$_{SARS2}$ + F490S$_{SARS2}$). Together, these findings show that affinity
550 maturation raises the genetic barrier to viral escape, such that the virus must acquire multiple
551 coordinated epitope substitutions to overcome neutralization. As a result, affinity-matured
552 antibodies may sustain protective immunity over longer periods, underscoring their essential
553 role in maintaining durable immune protection.
554

555 In addition, C092, C807, BD56-104, and BD56-597 exhibit broad cross-reactivity with a
556 diverse panel of SARS-related coronavirus (SARSr-CoV) RBDs, including Pangolin-GD-
557 2019 [44], Bat-RaTG13, Pangolin-GX-2017 [45], Laos-20-52, Laos-20-236 [46], Bat-RsSHC014,
558 Bat-WIV1[47], SARS-CoV-1[48,49], BtKY72, GX2013, HeB2013, and RmYN02 [38]. This
559 substantial expansion in breadth indicates that affinity maturation not only enhances tolerance
560 to SARS-CoV-2 epitope mutations but also extends the reactivity of R1-32-like antibodies to
561 antigenically diverse sarbecoviruses. The likely presence of such affinity-matured public
562 antibodies further suggests that a degree of pre-existing immunity to diverse sarbecoviruses
563 may now be present in the human population after the SARS-CoV-2 pandemic. The finding
564 that affinity maturation broadens antibody reactivity toward heterologous sarbecoviruses,
565 with substantially diverged epitopes, provides a conceptual framework for new strategies to
566 design and discover broadly neutralizing antibodies that do not necessarily rely on targeting
567 highly conserved epitopes.
568
569 Furthermore, structural characterization of affinity matured R1-32-like public antibodies
570 revealed specific mutations relative to germline R1-32-like antibodies in and around the CDR
571 loops, including $A33F_H$, $N59D_H$, $Q62E_H$, $A109Y_H$, $S26D_L$, $G70D_L$, and $G99D_L$, that enhance
572 antigen binding, increase resilience to epitope mutations, and expand antibody breadth.
573 Notably, many of these sites (33_H, 59_H, 62_H, and 26_L) coincide with SHM-enriched sites in
574 R1-32-like antibodies that tolerate BQ.1.1 ($L452R_{SARS2}$) and XBB ($F490S_{SARS2}$), suggesting
575 convergent affinity-maturation patterns that promote increased resilience to antigenic drift.
576 We confirmed this concept by introducing mutations at these seven sites into R1-32 to
577 generate an artificially affinity-matured variant, R1-32-AAM, which exhibits improved
578 tolerance to the $L452_{SARS2}$ and $F490_{SARS2}$ mutations. These findings demonstrate how
579 deciphering in vivo maturation patterns can guide in vitro maturation strategies to enhance
580 antibody potency for therapeutic applications, as previously envisioned [50].
581
582 R1-32-like public antibodies utilize their characteristic IGHV1-69 germline-encoded
583 hydrophobic HCDR2 loops to bind a convergent epitope on the SARS-CoV-2 RBD, defined
584 by a hydrophobic patch formed by residues $L452_{SARS2}$, $F490_{SARS2}$, and $L492_{SARS2}$ [16,27]. Likely
585 owing to selection pressure from R1-32-like and other IGHV1-69 antibodies, residues
586 $L452_{SARS2}$ and $F490_{SARS2}$ have become antigenic mutation hotspots [16,51,52], impairing antigen
587 binding for most early-isolated R1-32-like antibodies that retained germline-like sequences
588 and lacked extensive affinity maturation [16,27]. The identification of R1-32-like antibodies that
589 are tolerant to epitope mutations implies that members of this class likely remain active in the
590 population and continue to exert immune pressure on this site. The emergence of the novel
591 $N354_{SARS2}$ glycosylation may reflect a viral adaptation to this pressure, highlighting viral
592 evolution potentially driven by this class of public antibodies.
593

Since the emergence of the BA.2.86 variant (**Fig. S16b**), the $N354_{SARS2}$ glycosylation mutation has become fixed in circulating strains [41,43]. We have shown that the synergistic effect of sequence variation and glycan-mediated structural occlusion enables viral escape from previously identified mutation-tolerant R1-32-like antibodies (C092, C807, BD56-104, and BD56-597). To identify antibodies with even stronger mutation-tolerance, we applied AI-driven antibody language modelling and discovered an ultrapotent antibody, ZL525, which retains strong neutralizing activity against the KP.3 variant carrying the $N354_{SARS2}$ glycosylation. Structural analysis indicates that SHM-introduced smaller or more flexible hydrophobic residues ($L/F55A_H$ and $I/T57M_H$) in HCDR2 likely confer enhanced conformational adaptability, allowing ZL525 to engage the altered hydrophobic surface formed by $F490_{SARS2}$, $L492_{SARS2}$, and more importantly the substituted $L452W_{SARS2}$ (**Fig. 6f**), while counteracting the shielding effect of the newly introduced $N354_{SARS2}$ glycan. Moreover, ZL525 extends cross-reactivity to the SARS-CoV-1 S-protein, which is substantially diverged from SARS-CoV-2. Together, these findings indicate that affinity maturation can further evolve R1-32-like antibodies to acquire breadth that not only counters viral escape but also enables cross-reactivity to more divergent sarbecoviruses.

The successful discovery of the ultrapotent broadly neutralizing antibody ZL525 through AI-driven language modelling highlights the transformative potential of machine learning in accelerating antibody discovery. By decoding the functional patterns of somatic hypermutations (SHMs) that confer broad neutralization, our study demonstrates how AI can systematically infer critical sequence-structure-function relationships that might otherwise require extensive experimental screening [53]. This approach is particularly powerful for targeting rapidly evolving pathogens, like SARS-CoV-2, where conventional antibody discovery methods struggle to keep pace with viral escape variants [54]. Recent advances in deep learning-based protein modelling, such as AlphaFold and antibody-specific language models, have begun to bridge the gap between sequence analysis and functional prediction [54]. Future integration of structural constraints with generative AI could further enhance the precision of antibody optimization [55], paving the way for rapid discovery of antibody therapeutics to counter emerging viral threats. Together, these findings illustrate the dynamic interplay between population-level antibody responses and viral antigenic evolution, and highlight how integrating mechanistic immunology with AI-driven discovery can accelerate the development of antibodies resilient to rapidly evolving pathogens.

629 **Methods**

630 **COVID-19 patient and vaccine recipient enrollment**

631 Between December 2022 and December 2023, we enrolled a cohort of 64 individuals with
632 RT-PCR-confirmed SARS-CoV-2 infection. All participants had received three doses of an
633 inactivated COVID-19 vaccine (Sinopharm or CoronaVac) before experiencing sequential
634 breakthrough infections with the BA.5 and XBB subvariants, which corresponded to the two
635 major epidemic waves during this period. All participants provided written informed consent
636 before enrollment. The study was conducted under the approval and supervision of the Ethics
637 Committee of the First Affiliated Hospital of Guangzhou Medical University (Ethics IDs: ES-
638 2020-65).

639 **Cells and viruses**

640 Expi293F cells (Thermo Fisher Scientific, Cat# A14527) were cultured in FreeStyle^{TM}293
641 Expression Medium (Thermo Fisher Scientific, Cat# A1435101) in a shaking incubator at
642 37 °C with 8% CO_2. Human embryonic kidney (HEK) 293T (ATCC, Cat# CRL-3216),
643 HEK293T-ACE2, and Vero E6 cells (ATCC, Cat# CRL-1586) were cultured in 10% FBS-
644 supplemented Dulbecco's Modified Eagle's Medium (DMEM) at 37°C, 5% CO_2. Expi293F
645 cells were used for recombinant protein expression. HEK293T cells were used to generate
646 VSV-based pseudoviruses, while HEK293T-ACE2 and Vero E6 cells were used for
647 neutralization assays. VSV-based pseudotyped viruses were generated as previously
648 described [36]. Authentic SARS-CoV-2 viruses, including WT, Beta, Delta, and Omicron
649 (BA.1, BA.4/5, BQ.1, XBB.1, EG.5, and KP.3), were isolated from clinical specimens of
650 COVID-19 patients and stored at the Guangzhou Customs District Technology Center BSL-3
651 laboratory. The SARS-CoV-2 Delta strain was kindly provided by the Guangdong Provincial
652 Center for Disease Control and Prevention, China. All experiments involving authentic
653 SARS-CoV-2 were conducted under biosafety level 3 (BSL-3) conditions at the Guangzhou
654 Customs District Technology Center BSL-3 Laboratory.
655

656 **Expression and purification of human monoclonal antibodies**

657 The heavy chain (IgH) and light chain (IgL) genes of antibodies were amplified and cloned
658 into the expression vector pCMV3 using ClonExpress Ultra One Step Cloning Kit (Vazyme,
659 C115). When the density of Expi293F cells reached 2.5×10^6 cells/mL, the paired IgH and
660 IgL plasmids were transiently co-transfected into the cells at a ratio of 1:1 using transfection
661 reagent Polyethylenimine (PEI). The transfected cells were transferred to a shaking incubator
662 at 33 °C with 8% CO_2. Five days post-transfection, the IgG was purified from the cell
663 supernatant using protein A affinity chromatography. Firstly, the supernatant was harvested
664 by centrifugation and incubated with Protein A Resin (Genscript, China) for 2 h to enable
665 antibody binding. After the resin was washed with PBS (Gibco), pH 7.4, the IgG bound to the

666 resin was eluted using 0.1 M citric acid, pH 3.0, and neutralized immediately with an equal
667 volume of 1 M Tris-HCl, pH 8.0, to maintain the pH within the neutral range. Subsequently,
668 the fractions containing IgG were concentrated and buffer-exchanged into PBS (pH 7.4)
669 using a 50 kDa MWCO Amicon Ultra filtration device (Merck Millipore). Purified antibodies
670 were aliquoted, flash-frozen, and stored at -80 °C until needed.
671

672 **Fab fragment production**

673 To produce Fab gene fragment, the VH and the human IgG1 constant region CH1 were
674 amplified from the IgH gene. The plasmids of paired Fab-IgH and IgL were transiently co-
675 transfected into the Expi293F cells at a ratio of 1:1 using the transfection reagent
676 Polyethylenimine (PEI) when the cell density reached 2.5×10^6 cells/mL. Five days post-
677 transfection at 33 °C, the culture supernatant was collected by centrifugation and incubated
678 with LambdaFabSelect (Cytiva) resin for 2 h to enable Fab binding. After the resin was
679 washed with PBS, the Fab bound to the resin was eluted with 0.1 M glycine (pH 2.0) into
680 1/2th volume 1 M Tris-HCl, pH 8.0, to maintain the pH within the neutral range.
681 Subsequently, the target elutions were concentrated by a 30 kDa MWCO Amicon Ultra
682 filtration device (Merck Millipore). Finally, the Fab was further purified and buffer-
683 exchanged into PBS using a Superdex 200 increase 10/300 GL column (Cytiva). Purified Fab
684 was aliquoted, flash frozen, and stored at −80 °C until needed.
685

686 **Expression and purification of SARS-CoV-2 S trimer and RBD**

687 SARS-CoV-2 Omicron BA.4/5 S trimer ectodomain (14-1211) with HexaPro [56] mutations
688 (F817P, A892P, A899P, A942P, K986P, and V987P) and deletion of amino acids "PRRA"
689 (681-684) at the fusion site was constructed into the expression vector pCDNA3.1 with an N-
690 terminal μ-phosphatase signal peptide and a C-terminal TEV-cleavage site, a T4 foldon
691 trimerization motif, and a hexahistidine tag [57,58]. Various SARS-CoV-2 variants S trimer
692 ectodomain (S-R) with "PRRA" (681-684) deletion at the fusion site were also constructed
693 using the same method. The coding sequence of SARS-CoV-2 RBD (residues 332-527) with
694 an N-terminal μ-phosphatase signal peptide and a C-terminal hexahistidine tag was cloned
695 into the expression vector pCDNA3.1 [57]. All expression plasmids of S-trimer and RBD were
696 transiently transfected into Expi293F cells using transfection reagent Polyethylenimine [59].
697 Five days post-transfection at 33 °C, the cultural supernatant was collected and supplemented
698 with 25 mM phosphate, pH 8.0, 300 mM NaCl, 5 mM imidazole, and 0.5 mM PMSF
699 recirculated onto a HiTrap TALON crude column (Cytiva). Subsequently, the column was
700 washed with buffer A (25 mM phosphate, pH 8.0, 300 mM NaCl, 5 mM imidazole), and
701 target protein was eluted with a 100 mL linear gradient to 100% buffer B (25 mM phosphate,
702 pH 8.0, 300 mM NaCl, 500 mM imidazole). Fractions containing the target protein were
703 concentrated with an MWCO Amicon Ultra filtration device (Merck Millipore) and buffer-

704 exchanged into PBS. Additionally, all RBDs were further purified and buffer-exchanged into
705 PBS using a Superdex 75 increase 10/300 GL column (Cytiva) to remove RBD dimers. All
706 SARS-CoV-2 spike and RBD variants were purified as described above. Purified S-trimers
707 and RBDs were aliquoted, flash frozen, and stored at -80 °C until needed.
708

709 **Binding kinetics and affinity assessment of antibodies by BLI**

710 Binding kinetics and affinities of mAbs against SARS-CoV-2 spikes or RBDs and SARSr-
711 CoVs RBDs were assessed by Biolayer Interferometry (BLI) on an Octet RED96 instrument
712 (FortéBio, USA). The assays were performed at 25 °C, and all proteins were diluted to PBST
713 buffer (PBS with 1mg/mL BSA and 0.02% v/v Tween-20). Biosensors were pre-equilibrated
714 in the PBST buffer for 10 min before the experiments. Initially, antibodies (11 μg/mL) were
715 immobilized onto Protein A biosensors to a level of ~1.5 nm. After a 60 s baseline step in
716 PBST buffer, biosensors loaded with mAb were exposed (300 s) to the spikes (from 200 nM
717 to 3.125 nM in 2-fold serial dilutions) or various RBDs (200 nM) to measure association.
718 Subsequently, the biosensors were dipped into PBST (600 s) to measure dissociation of
719 spikes or RBDs from the biosensor surface. A blank reference was set for each reaction. Data
720 was reference-subtracted and analyzed using the FortéBio data analysis software HT
721 v12.0.2.59 (FortéBio) by fitting to single or double phase association and dissociation
722 kinetics to determine k_{on}, k_{off} and K_D. Raw data and fit data were plotted in GraphPad Prism
723 8.0.
724

725 **Antibody competition assay by BLI**

726 The competitive assays between antibodies or between antibodies and ACE2 were measured
727 by Biolayer Interferometry (BLI) using an Octet RED96 instrument (FortéBio, USA). All
728 experimental steps were performed at 25 °C. All proteins were diluted to PBST buffer (PBS
729 with 1mg/mL BSA and 0.02% v/v Tween-20), and anti-His biosensors were pre-equilibrated
730 in PBST buffer for 10 min before being immobilized with purified SARS-CoV-2 RBD-His
731 protein (30 μg/mL). Biosensors loaded with RBD were saturated with the first ligand
732 (antibodies or ACE2 with a concentration of 200nM), and then binding of the second ligand
733 (antibodies or ACE2 with a concentration of 200nM) or buffer as control was measured for
734 300 s. Data was analyzed using the FortéBio data analysis software HT v12.0.2.59 (FortéBio)
735 and raw data was plotted in GraphPad Prism 8.0.
736

737 **Pseudovirus neutralization assay**

738 The neutralization potency of antibodies against SARS-CoV-2 wild-type and multiple
739 variants (including Delta, Lambda, and Omicron sublineages BA.1, BA.2, BA.4/5,
740 BA.2.75.2, BQ.1.1, and EG.5) was evaluated using a pseudovirus neutralization test
741 following established protocols [36]. The antibody samples were diluted to an initial

742 concentration of 10 μg/mL and subjected to eight gradient dilutions (3× serial dilutions),
743 while the pseudovirus was diluted to 1.3×10^4 $TCID_{50}$/mL. After incubating the antibody
744 samples and pseudovirus at 37 °C for 1 hour, HEK293T-ACE2 cells were added. After 24
745 hours of culture, luciferase detection reagent was added and placed in the multifunctional
746 micropore detector (PE Ensight) to read the luminous value. Results were analyzed, and IC_{50}
747 values were calculated by GraphPad Prism 8.0.
748

749 **Authentic virus neutralization assay**

750 All experiments involving authentic SARS-CoV-2 virus were conducted under biosafety
751 level 3 (BSL-3) containment at the Guangzhou Customs District Technology Center.
752 Antibodies were initially diluted to 100 μg/mL and then subjected to 4-fold serial dilutions.
753 Each diluted mAb sample was combined with an equal volume of virus suspension
754 containing 200 focus-forming units (FFU) of specified SARS-CoV-2 strains (WT, Beta,
755 Delta, and Omicron subvariants BA.1, BA.4/5, BQ.1, XBB.1, EG.5, and KP.3). Mixtures
756 were added to Vero E6 cells in 96-well cell culture plates for 1 h at 37 °C. After removal of
757 the mixtures, fresh overlay medium consisting of MEM supplemented with 1.2%
758 carboxymethylcellulose was added to each well. Following 24 hours of incubation, the
759 overlay was discarded, and the cells were fixed with 4% paraformaldehyde (Biosharp, China,
760 Cat# BL539A) and permeabilized using 0.2% Triton X-100 (Sigma, USA, Cat# T8787).
761 Cells were incubated with a human anti-SARS-CoV-2 nucleocapsid protein monoclonal
762 antibody (obtained by laboratory screening) at 37 °C for 1 h. After three washes with 0.15%
763 PBST, cells were incubated with an HRP-labeled goat anti-human secondary antibody
764 (Jackson ImmunoResearch Laboratories, Cat# 609-035-213) at 37 °C for 1 h. Following
765 additional washes, foci were developed using TrueBlue Peroxidase Substrate (KPL,
766 Gaithersburg, MD, Cat# 50-78-02), and counted with an ELISPOT reader (Cellular
767 Technology Ltd. Cleveland, OH). The foci reduction neutralization test titer ($FRNT_{50}$) was
768 calculated by the SpearmanKarber method.
769

770 **Cryo-EM sample preparation and data collection**

771 The BA.4/5 S-R/6P S-trimer was mixed with the corresponding Fab and ACE2 at a 3(S-
772 protomer):3(Fab):3(ACE2) molar ratio for 1 minute to form the C092, C807, BD56-104, and
773 BD56-597 Fab complexes. Similarly, the GX2013 S-trimer was mixed with C092 and D1H4,
774 and the LP.8.1 S-trimer was mixed with ZL525 and ZL58, each at a 3:3:3 molar ratio for 1
775 minute to assemble the C092 Fab:D1H4 Fab:GX2013 S-trimer and ZL525 Fab:ZL58
776 Fab:LP.8.1 S-R/6P complexes, respectively. All mixtures contained 0.1% octyl glucoside,
777 except for the C092 Fab:D1H4 Fab:GX2013 complex, which contained 0.05% octyl
778 glucoside. Samples were loaded onto freshly glow-discharged (15 mA, 30 s) holey carbon
779 grids (Quantifoil, Cu R1.2/R1.3) at 4 °C and 100% humidity. The grids were blotted for 2.5 s

780 with a force of 4 and samples were frozen immediately in liquid ethane using a Vitrobot
781 (Thermo Fisher).
782
783 For the C092 Fab:ACE2:Omicron BA.4/5 S-R/6P and C092 Fab:D1H4 Fab:GX2013 S-trimer
784 complexes, cryo-EM data were collected using a 200 keV Talos Arctica electron microscope
785 (ThermoFisher Scientific) equipped with a K3 direct electron detector (Gatan). Movies were
786 recorded using the SerialEM version 3.8.7 software at a nominal magnification of 45,000×
787 with a calibrated pixel size of 0.88 Å and a defocus range from -0.8 to -2.5 µm. Samples were
788 exposed for 1.83 s with a dose rate of 25.4 e^-/pixel/s fractionated over 27 frames, giving a
789 total electron dose of 60 $e^-/Å^2$.
790
791 To achieve higher resolution, a separately prepared C092 Fab:ACE2:BA.4/5 S-R/6P complex
792 was additionally imaged in a Titan Krios electron microscope (Thermo Fisher Scientific)
793 operating at 300 keV equipped with a SelectrisX energy filter (slit width 10 eV) and a Falcon
794 4 direct electron detector. The C807, BD56-104, and BD56-597 complexes, as well as the
795 ZL525 Fab:ZL58 Fab:LP.8.1 S-R/6P complex, were also imaged in the Titan Krios electron
796 microscope under the same setup. Movie stacks were automatically recorded using EPU with
797 the electron event representation (EER) mode at a nominal magnification of ×165,000 with a
798 calibrated pixel size of 0.73 Å and nominal defocus values ranging between -0.6 to -2.0 µm.
799 Each stack was recorded and exposed at a dose rate of 6.53 e−/pixel/s for 4.08 s resulting a
800 total dose of ~ 50 $e^-/Å^2$. All movie stacks were imported into cryoSPARC live
801 (v3.3.2/v4.2.0) [60] for pre-processing, which includes patched motion correction, contrast
802 transfer function (CTF) estimation, and bad image rejection.
803

804 ## Cryo-EM data processing

805 Data processing was carried out using cryoSPARC v3.3.2/v4.2.0. After removing bad
806 images, particles were picked by blob-picking on images and extracted for 2D Classification.
807 Well-defined 2D classes were selected as templates for template-picking.
808
809 For the C092 Fab:ACE2:BA.4/5 S-R/6P dataset collected at 200 keV **(Fig. S5)**, template-
810 picked particles were extracted and subjected to two rounds of 2D classification to remove
811 low-quality particles. Particles of either disassembled spike (S1) or Fab bound S-trimers were
812 separated by 2D classification into two sub-datasets. For the S1 sub-dataset, Ab-initio
813 Reconstruction was performed to generate initial 3D models, before the selected models were
814 used as references in Heterogeneous Refinement. A well-defined structure was constructed
815 by Non-uniform Refinement. To improve local resolution, a soft mask was applied to the
816 ACE2:RBD:Fab interface for Local Refinement, yielding a final map at 3.84 Å resolution.
817 For the S-trimer sub-dataset, three rounds of Ab-initial Reconstruction were conducted to
818 remove bad particles. All resulting models from the final round were used as references in

Heterogeneous Refinement. Particles generating highly similar structures were combined and subject to Non-uniform Refinement. This process yielded two distinct S-trimer reconstructions, featuring either 2 or 3 RBD "up" conformations, allowing simultaneous binding of either 2 or 3 Fab and ACE2 molecules.

To improve resolution, a separate C092 Fab:ACE2:BA.4/5 S-R/6P complex dataset was collected on a Titan Krios operating at 300 keV **(Fig. S6)**. Template-picked particles were similarly split into S1 and S-trimer subsets via 2D classification. For the S1 sub-dataset, Ab-initio Reconstruction and Heterogeneous Refinement were performed to generate 3D reconstructions. To improve reconstruction, Topaz Training and Picking was performed before picked particles were subjected to 2D Classification, Ab-initio Reconstruction, and Heterogeneous Refinement again. The final particles were subjected to Non-uniform Refinement, followed by Local Refinement with a mask focused on the ACE2:RBD:Fab interface regions to yield a final map at 2.58 Å resolution. For the S-trimer sub-dataset collected at 300 keV, A good 3D reconstruction was not obtained due to the absence of side-view projections in 2D classes, even after Topaz picking.

For the C807/BD56-104/BD56-597 Fab:ACE2:BA.4/5 S-R/6P datasets **(Figs. S6 and S7)**, Template-picked particles were similarly divided into two sub-datasets. The S1 sub-datasets were processed in a workflow identical to the C092 Fab:ACE2:BA.4/5 S-R/6P S1 sub-dataset collected at 300 keV. The S-trimer sub-datasets were processed using similar workflows, each yielding a structure showing a S-trimer simultaneously bound by three Fabs and three ACE2s. For the C807 Fab bound S-trimer sub-dataset, Topaz training was performed to further pick S-trimer particles. The Topaz picked particles were subjected to 2D Classification, Ab-initio Reconstruction, Heterogeneous Refinement, and Non-uniform Refinement to reconstruct a final map. For the BD56-104 Fab bound S-trimer sub-dataset, Topaz training and picking was performed after Heterogeneous Refinement. For the BD56-597 S-trimer sub-dataset, reconstruction was obtained without performing Topaz picking.

For the C092 Fab:D1H4 Fab:GX2013 dataset collected at 200 keV **(Fig. S14)**, Fab bound S1 particles from disassembled S-trimers were template-picked before subjecting to 2D Classification, Ab-initio Reconstruction, and Homogeneous Refinement. Topaz training and picking were performed to further pick particles. The final reconstruction was obtained using Topaz picked particles using Non-uniform Refinement, with a resolution of 3.45 Å.

For the ZL525 Fab:ZL58 Fab:LP.8.1 S-R/6P dataset **(Fig. S15)**, only Fab bound S-trimers were observed by auto-picking and subsequent 2D classification. S-trimer particles were subject to Ab-initio Reconstruction, Homogeneous Refinement, and Non-uniform Refinement, imposing C3 symmetry to generate a map with a resolution of 2.75 Å. To improve the resolution of the RBD:Fab interfaces, 3D classification with a focused mask

859 (ZL525 Fab:ZL58 Fab:LP.8.1 RBD) was applied to remove low-quality particles, followed
860 by Local Refinement. Ultimately, the focused ZL525 Fab:ZL58 Fab:LP.8.1 RBD map was
861 refined to a resolution of 2.93 Å.
862
863 All resolutions were estimated at the 0.143 criterion from phase-randomization-corrected
864 Fourier shell correlation (FSC) curves calculated between two independently refined half-
865 maps, multiplied by soft-edged solvent masks, in either RELION v4.0 or cryoSPARC [60].
866 Additional data processing details are summarized in **Figs. S5-8** and **Table S9**.
867

868 ## Cryo-EM model building and structure refinement

869 A previously determined structure of R1-32 Fab:ACE2:SARS-CoV-2 RBD complex (PDB:
870 7YDI) was fitted into the Cryo-EM map in UCSF Chimera v1.15 [61] and used as the starting
871 model for model building of the four complexes (C092/C807/BD56-104/BD56-597
872 Fab:ACE2:Omicron BA.4/5 RBD. Manual model building was carried out in Coot [62] in order
873 to adjust Ramachandran, rotamers, bond geometry restraints, etc. Structure refinement was
874 performed automatically using real-space refinement in PHENIX [63]. For C092/C807/BD56-
875 104/BD56-597 Fab:ACE2:Omicron BA.4/5 S-timer complexes, the structures
876 (PDB:7YE5/7YEG) were used as initial model. For C092 Fab:D1H4 Fab:GX2013 RBD and
877 ZL525 Fab:ZL58 Fab LP.8.1 RBD complexes, the structures (PDB:8ZY6 and 8WXL) were
878 used as initial model respectively. Model validation statistics were summarized in **Table S9**.
879

880 ## Ligand-induced conformational change assay

881 SARS-CoV-2 S-R spike at 1 mg/mL (7.09 μM) was incubated with ACE2-Fc or antibodies at
882 a 1:1.1 molar ratio for 1 h at room temperature. The samples were subsequently treated with
883 50 μg/mL proteinase K for 30 min at 4 °C. Non-reducing SDS-PAGE loading buffer (5×) was
884 added to each sample immediately before boiling at 98 °C for 5 min to stop the reaction.
885 Samples were separated by SDS–PAGE and transferred onto a PVDF membrane. After
886 blocking with 5% (w/v) skimmed milk in TBST buffer, the membrane was incubated with a
887 rabbit anti-SARS-CoV-2 S2 polyclonal antibody (1:2,500 dilution, Sino Biological, 40590-
888 T62) and subsequently with a goat anti-rabbit IgG conjugated to horseradish peroxidase
889 (1:1,000 dilution, Beyotime, A0208). The S proteins on the membrane were detected by
890 chemical luminescence using Pierce ECL western blotting substrate (Thermo Fisher, 32106).
891 To further assess the effect of non-ACE2 competing antibodies on S-R spike conformation,
892 the S-R spike protein was pre-incubated with antibodies (1 h), followed by incubation with
893 ACE2-Fc (1 h). Samples were analyzed by western blotting as described above.
894

895 **Pre-trained antibody language models, ESM2 model, and virtual screening**

896 Similar to our previously described Ab2binder model [31], we pre-trained antibody-specific
897 language models on 1.4 billion antibody sequences sourced from the OAS database. After
898 removing duplicate sequences and those containing non-canonical amino acids, the curated
899 dataset consisted of 1.2 billion heavy chain and 210 million light chain sequences. Using the
900 RoFormer [39] architecture, separate models were pre-trained for heavy and light chains. A
901 Unique Amino Acid (UAA) tokenizer was adopted to represent each residue as a discrete
902 token. Self-supervised learning was performed via a Masked Amino Acid (MAA) objective,
903 in which randomly obscured residues were predicted from contextual cues, enabling the
904 model to infer structural and functional properties of antibody sequences. To represent
905 antigen inputs, we utilized the evolutionary-scale language model ESM2 (150M parameters),
906 pre-trained on UniRef50 [64], to capture deep phylogenetic and structural features from protein
907 sequences. Antigen embeddings were derived from ESM2 to encode functional constraints
908 across diverse protein families. For antibody–antigen binding affinity prediction, features
909 from both antibody chains, extracted using our pre-trained antibody models, were combined
910 with ESM2-derived antigen embeddings. These representations were integrated via a multi-
911 layer perceptron (MLP) to estimate binding affinities. The model was fine-tuned on a
912 consolidated affinity dataset assembled from multiple public sources [1,12,28,32,33,65-68],
913 enhancing its capacity to discern subtle interactions between antibodies and antigenic
914 variants. Finally, we applied the optimized model to screen a library of 190 R1-32-like
915 monoclonal antibodies in silico, of which 102 antibodies were derived from published data
916 and 88 antibodies were isolated from convalescent individuals. Detailed information on
917 isolating the latter set of antibodies will be described in a separate study [69]. Candidates were
918 ranked by predicted affinity, and top-scoring antibodies were prioritized for experimental
919 validation.
920

921 **Reference**

922 1 Cao, Y. *et al.* Imprinted SARS-CoV-2 humoral immunity induces convergent Omicron
923 RBD evolution. *Nature* **614**, 521-529, doi:10.1038/s41586-022-05644-7 (2023).
924 2 Murin, C. D., Wilson, I. A. & Ward, A. B. Antibody responses to viral infections: a
925 structural perspective across three different enveloped viruses. *Nat Microbiol* **4**, 734-
926 747, doi:10.1038/s41564-019-0392-y (2019).
927 3 Cao, Y. *et al.* Potent Neutralizing Antibodies against SARS-CoV-2 Identified by High-
928 Throughput Single-Cell Sequencing of Convalescent Patients' B Cells. *Cell* **182**, 73-
929 84.e16, doi:10.1016/j.cell.2020.05.025 (2020).
930 4 Liu, Y. *et al.* The N501Y spike substitution enhances SARS-CoV-2 infection and
931 transmission. *Nature* **602**, 294-299, doi:10.1038/s41586-021-04245-0 (2022).
932 5 Mannar, D. *et al.* Structural analysis of receptor binding domain mutations in SARS-
933 CoV-2 variants of concern that modulate ACE2 and antibody binding. *Cell Rep* **37**,
934 110156, doi:10.1016/j.celrep.2021.110156 (2021).
935 6 Wang, R. *et al.* Analysis of SARS-CoV-2 variant mutations reveals neutralization
936 escape mechanisms and the ability to use ACE2 receptors from additional species.
937 *Immunity* **54**, 1611-1621.e1615, doi:10.1016/j.immuni.2021.06.003 (2021).
938 7 Yuan, M. *et al.* Structural and functional ramifications of antigenicdrift in recent
939 SARS-CoV-2 variants. *science* (2021).
940 8 Mannar, D. *et al.* SARS-CoV-2 Omicron variant: Antibody evasion and cryo-EM
941 structure of spike protein-ACE2 complex. *Science* **375**, 760-764,
942 doi:10.1126/science.abn7760 (2022).
943 9 Barnes, C. O. *et al.* SARS-CoV-2 neutralizing antibody structures inform therapeutic
944 strategies. *Nature* **588**, 682-687, doi:10.1038/s41586-020-2852-1 (2020).
945 10 Sokal, A. *et al.* Maturation and persistence of the anti-SARS-CoV-2 memory B cell
946 response. *Cell* **184**, 1201-1213.e1214, doi:10.1016/j.cell.2021.01.050 (2021).
947 11 Yuan, M. *et al.* Structural basis of a shared antibody response to SARS-CoV-2. *Science*
948 **369**, 1119-1123, doi:10.1126/science.abd2321 (2020).
949 12 Muecksch, F. *et al.* Affinity maturation of SARS-CoV-2 neutralizing antibodies confers
950 potency, breadth, and resilience to viral escape mutations. *Immunity* **54**, 1853-1868
951 e1857, doi:10.1016/j.immuni.2021.07.008 (2021).
952 13 Chen, E. C. *et al.* Convergent antibody responses to the SARS-CoV-2 spike protein in
953 convalescent and vaccinated individuals. *Cell Rep* **36**, 109604,
954 doi:10.1016/j.celrep.2021.109604 (2021).
955 14 Yan, Q. *et al.* Antibodies utilizing VL6-57 light chains target a convergent cryptic
956 epitope on SARS-CoV-2 spike protein and potentially drive the genesis of Omicron
957 variants. *Nat Commun* **15**, 7585, doi:10.1038/s41467-024-51770-3 (2024).
958 15 Zhang, Y. *et al.* Analysis of B Cell Receptor Repertoires Reveals Key Signatures of the
959 Systemic B Cell Response after SARS-CoV-2 Infection. *J Virol* **96**, e0160021,
960 doi:10.1128/jvi.01600-21 (2022).
961 16 Yan, Q. *et al.* Shared IGHV1-69-encoded neutralizing antibodies contribute to the
962 emergence of L452R substitution in SARS-CoV-2 variants. *Emerg Microbes Infect* **11**,
963 2749-2761, doi:10.1080/22221751.2022.2140611 (2022).
964 17 Patel, A. *et al.* Molecular basis of SARS-CoV-2 Omicron variant evasion from shared
965 neutralizing antibody response. *Structure* **31**, 801-811.e805,
966 doi:10.1016/j.str.2023.04.010 (2023).

18 Kaku, C. I. *et al.* Evolution of antibody immunity following Omicron BA.1 breakthrough infection. *Nat Commun* **14**, 2751, doi:10.1038/s41467-023-38345-4 (2023).
19 Yan, Q. *et al.* Germline IGHV3-53-encoded RBD-targeting neutralizing antibodies are commonly present in the antibody repertoires of COVID-19 patients. *Emerg Microbes Infect* **10**, 1097-1111, doi:10.1080/22221751.2021.1925594 (2021).
20 Zhang, Q. *et al.* Potent and protective IGHV3-53/3-66 public antibodies and their shared escape mutant on the spike of SARS-CoV-2. *Nat Commun* **12**, 4210, doi:10.1038/s41467-021-24514-w (2021).
21 Rapp, M. *et al.* Modular basis for potent SARS-CoV-2 neutralization by a prevalent VH1-2-derived antibody class. *Cell Rep* **35**, 108950, doi:10.1016/j.celrep.2021.108950 (2021).
22 Liu, B. *et al.* An unconventional VH1-2 antibody tolerates escape mutations and shows an antigenic hotspot on SARS-CoV-2 spike. *Cell Rep* **43**, 114265, doi:10.1016/j.celrep.2024.114265 (2024).
23 Dong, J. *et al.* Genetic and structural basis for SARS-CoV-2 variant neutralization by a two-antibody cocktail. *Nat Microbiol* **6**, 1233-1244, doi:10.1038/s41564-021-00972-2 (2021).
24 Yuan, M. *et al.* Molecular analysis of a public cross-neutralizing antibody response to SARS-CoV-2. *Cell Rep* **41**, 111650, doi:10.1016/j.celrep.2022.111650 (2022).
25 Wang, Y. *et al.* A large-scale systematic survey reveals recurring molecular features of public antibody responses to SARS-CoV-2. *Immunity* **55**, 1105-1117.e1104, doi:10.1016/j.immuni.2022.03.019 (2022).
26 Westendorf, K. *et al.* LY-CoV1404 (bebtelovimab) potently neutralizes SARS-CoV-2 variants. *Cell Rep* **39**, 110812, doi:10.1016/j.celrep.2022.110812 (2022).
27 He, P. *et al.* SARS-CoV-2 Delta and Omicron variants evade population antibody response by mutations in a single spike epitope. *Nat Microbiol* **7**, 1635-1649, doi:10.1038/s41564-022-01235-4 (2022).
28 Cao, Y. *et al.* BA.2.12.1, BA.4 and BA.5 escape antibodies elicited by Omicron infection. *Nature* **608**, 593-602, doi:10.1038/s41586-022-04980-y (2022).
29 Wang, Q. *et al.* Alarming antibody evasion properties of rising SARS-CoV-2 BQ and XBB subvariants. *Cell* **186**, 279-286.e278, doi:10.1016/j.cell.2022.12.018 (2023).
30 Tegally, H. *et al.* Emergence of SARS-CoV-2 Omicron lineages BA.4 and BA.5 in South Africa. *Nat Med* **28**, 1785-1790, doi:10.1038/s41591-022-01911-2 (2022).
31 He, H. *et al.* De novo generation of SARS-CoV-2 antibody CDRH3 with a pre-trained generative large language model. *Nat Commun* **15**, 6867, doi:10.1038/s41467-024-50903-y (2024).
32 Gaebler, C. *et al.* Evolution of antibody immunity to SARS-CoV-2. *Nature* **591**, 639-644, doi:10.1038/s41586-021-03207-w (2021).
33 Wang, Z. *et al.* Naturally enhanced neutralizing breadth against SARS-CoV-2 one year after infection. *Nature* **595**, 426-431, doi:10.1038/s41586-021-03696-9 (2021).
34 Wang, Z. *et al.* mRNA vaccine-elicited antibodies to SARS-CoV-2 and circulating variants. *Nature* **592**, 616-622, doi:10.1038/s41586-021-03324-6 (2021).
35 Zhang, L. *et al.* A proof of concept for neutralizing antibody-guided vaccine design against SARS-CoV-2. *Natl Sci Rev* **8**, nwab053, doi:10.1093/nsr/nwab053 (2021).

36 Nie, J. *et al.* Quantification of SARS-CoV-2 neutralizing antibody by a pseudotyped virus-based assay. *Nat Protoc* **15**, 3699-3715, doi:10.1038/s41596-020-0394-5 (2020).
37 Yu, H. *et al.* Somatically hypermutated antibodies isolated from SARS-CoV-2 Delta infected patients cross-neutralize heterologous variants. *Nat Commun* **14**, 1058, doi:10.1038/s41467-023-36761-0 (2023).
38 Wang, J. *et al.* SARS-related coronavirus S-protein structures reveal synergistic RBM interactions underpinning high-affinity human ACE2 binding. *Sci Adv* **11**, eadr8772, doi:10.1126/sciadv.adr8772 (2025).
39 Su, J. *et al.* RoFormer: Enhanced transformer with Rotary Position Embedding. *Neurocomputing* **568**, 127063, doi:https://doi.org/10.1016/j.neucom.2023.127063 (2024).
40 Lin, Z. *et al.* Evolutionary-scale prediction of atomic-level protein structure with a language model. *Science* **379**, 1123-1130, doi:10.1126/science.ade2574 (2023).
41 Li, L. *et al.* Spike structures, receptor binding, and immune escape of recently circulating SARS-CoV-2 Omicron BA.2.86, JN.1, EG.5, EG.5.1, and HV.1 sub-variants. *Structure* **32**, 1055-1067.e1056, doi:10.1016/j.str.2024.06.012 (2024).
42 Yang, H. *et al.* Structural basis for the evolution and antibody evasion of SARS-CoV-2 BA.2.86 and JN.1 subvariants. *Nat Commun* **15**, 7715, doi:10.1038/s41467-024-51973-8 (2024).
43 Liu, P. *et al.* Spike N354 glycosylation augments SARS-CoV-2 fitness for human adaptation through structural plasticity. *Natl Sci Rev* **11**, nwae206, doi:10.1093/nsr/nwae206 (2024).
44 Wrobel, A. G. *et al.* Structure and binding properties of Pangolin-CoV spike glycoprotein inform the evolution of SARS-CoV-2. *Nat Commun* **12**, 837, doi:10.1038/s41467-021-21006-9 (2021).
45 Zhang, S. *et al.* Bat and pangolin coronavirus spike glycoprotein structures provide insights into SARS-CoV-2 evolution. *Nat Commun* **12**, 1607, doi:10.1038/s41467-021-21767-3 (2021).
46 Ou, X. *et al.* Host susceptibility and structural and immunological insight of S proteins of two SARS-CoV-2 closely related bat coronaviruses. *Cell Discov* **9**, 78, doi:10.1038/s41421-023-00581-9 (2023).
47 Qiao, S. & Wang, X. Structural determinants of spike infectivity in bat SARS-like coronaviruses RsSHC014 and WIV1. *J Virol* **98**, e0034224, doi:10.1128/jvi.00342-24 (2024).
48 Zhang, X. *et al.* Disulfide stabilization reveals conserved dynamic features between SARS-CoV-1 and SARS-CoV-2 spikes. *Life Sci Alliance* **6**, doi:10.26508/lsa.202201796 (2023).
49 Yuan, Y. *et al.* Cryo-EM structures of MERS-CoV and SARS-CoV spike glycoproteins reveal the dynamic receptor binding domains. *Nat Commun* **8**, 15092, doi:10.1038/ncomms15092 (2017).
50 Vajda, S., Porter, K. A. & Kozakov, D. Progress toward improved understanding of antibody maturation. *Curr Opin Struct Biol* **67**, 226-231, doi:10.1016/j.sbi.2020.11.008 (2021).
51 Pushparaj, P. *et al.* Immunoglobulin germline gene polymorphisms influence the function of SARS-CoV-2 neutralizing antibodies. *Immunity*, doi:10.1016/j.immuni.2022.12.005 (2022).

52 Starr, T. N., Greaney, A. J., Dingens, A. S. & Bloom, J. D. Complete map of SARS-CoV-2 RBD mutations that escape the monoclonal antibody LY-CoV555 and its cocktail with LY-CoV016. *Cell Rep Med* **2**, 100255, doi:10.1016/j.xcrm.2021.100255 (2021).
53 Shan, S. *et al.* Deep learning guided optimization of human antibody against SARS-CoV-2 variants with broad neutralization. *Proc Natl Acad Sci U S A* **119**, e2122954119, doi:10.1073/pnas.2122954119 (2022).
54 Desautels, T. A. *et al.* Computationally restoring the potency of a clinical antibody against Omicron. *Nature* **629**, 878-885, doi:10.1038/s41586-024-07385-1 (2024).
55 Shanker, V. R., Bruun, T. U. J., Hie, B. L. & Kim, P. S. Unsupervised evolution of protein and antibody complexes with a structure-informed language model. *Science* **385**, 46-53, doi:10.1126/science.adk8946 (2024).
56 Hsieh, C. L. *et al.* Structure-based design of prefusion-stabilized SARS-CoV-2 spikes. *Science* **369**, 1501-1505, doi:10.1126/science.abd0826 (2020).
57 Xiong, X. *et al.* A thermostable, closed SARS-CoV-2 spike protein trimer. *Nat Struct Mol Biol* **27**, 934-941, doi:10.1038/s41594-020-0478-5 (2020).
58 Qu, K. *et al.* Engineered disulfide reveals structural dynamics of locked SARS-CoV-2 spike. *PLoS Pathog* **18**, e1010583, doi:10.1371/journal.ppat.1010583 (2022).
59 Yuan, H. *et al.* Structures and receptor binding activities of merbecovirus spike proteins reveal key signatures for human DPP4 adaptation. *Sci Adv* **11**, eadv7296, doi:10.1126/sciadv.adv7296 (2025).
60 Kucukelbir, A., Sigworth, F. J. & Tagare, H. D. Quantifying the local resolution of cryo-EM density maps. *Nat Methods* **11**, 63-65, doi:10.1038/nmeth.2727 (2014).
61 Pettersen, E. F. *et al.* UCSF Chimera--a visualization system for exploratory research and analysis. *J Comput Chem* **25**, 1605-1612, doi:10.1002/jcc.20084 (2004).
62 Emsley, P., Lohkamp, B., Scott, W. G. & Cowtan, K. Features and development of Coot. *Acta Crystallogr D Biol Crystallogr* **66**, 486-501, doi:10.1107/S0907444910007493 (2010).
63 Afonine, P. V. *et al.* Real-space refinement in PHENIX for cryo-EM and crystallography. *Acta Crystallogr D Struct Biol* **74**, 531-544, doi:10.1107/s2059798318006551 (2018).
64 Suzek, B. E., Wang, Y., Huang, H., McGarvey, P. B. & Wu, C. H. UniRef clusters: a comprehensive and scalable alternative for improving sequence similarity searches. *Bioinformatics* **31**, 926-932, doi:10.1093/bioinformatics/btu739 (2015).
65 Cao, Y. *et al.* Omicron escapes the majority of existing SARS-CoV-2 neutralizing antibodies. *Nature* **602**, 657-663, doi:10.1038/s41586-021-04385-3 (2022).
66 Wang, Z. *et al.* Memory B cell responses to Omicron subvariants after SARS-CoV-2 mRNA breakthrough infection in humans. *J Exp Med* **219**, doi:10.1084/jem.20221006 (2022).
67 Witte, L. *et al.* Epistasis lowers the genetic barrier to SARS-CoV-2 neutralizing antibody escape. *Nat Commun* **14**, 302, doi:10.1038/s41467-023-35927-0 (2023).
68 Kaku, C. I. *et al.* Recall of preexisting cross-reactive B cell memory after Omicron BA.1 breakthrough infection. *Sci Immunol* **7**, eabq3511, doi:10.1126/sciimmunol.abq3511 (2022).
69 Yan, Q. *et al.* AI recognizes convergent somatic hypermutation signatures to allow the discovery of variant-resilient broadly neutralizing antibodies. *bioRxiv*, 2025.2012.2010.693372, doi:10.64898/2025.12.10.693372 (2025).

Data availability

Cryo-EM density maps for the structures of R1-32-like antibodies in complex with S-trimer or S1 fragment have been deposited in the Electron Microscopy Data Bank (EMDB) with accession codes EMD-66890, EMD-66891, EMD-66892, EMD-66893, EMD-66894, EMD-66895, EMD-66896, EMD-66897, EMD-66898, EMD-66899, EMD-66900, and EMD-66901. Related atomic models have been deposited in the Protein Data Bank (PDB) under accession codes 9XHY, 9XHZ, 9XI0, 9XI1, 9XI2, 9XI3, 9XI4, 9XI5, 9XI6, 9XI7, 9XI8, and 9XI9, respectively.

Acknowledgements

We thank the staff of the GIBH-CAS Cryo-EM Facility for their help with cryo-EM sample preparation and data collection. We thank the staff of the Guangzhou Laboratory Cryo-EM Facility for their help with cryo-EM sample data collection. This work was supported by the National Key R&D Program of China (2021YFA1300903 to X.X.); the National Natural Science Foundation of China (82341085 and 32570199 to X.X., 82495200 and 82495203 to J.Z., 32361163669, 32170189, and 32241021 to J.H., 92469301 to L.C., 82201932 to Q.Y.); the Emergency Key Program of Guangzhou Laboratory (EKPG21-06 to X.X.); Major Project of Guangzhou National Laboratory (SRPG22-002 to X.X., EKPG21-30-2 to J.Z.); the Science and Technology Planning Project of Guangdong Province, China (2023B1212060050 and 2023B1212120009 to X.X.); the Basic Research Project of Guangzhou Institutes of Biomedicine and Health, Chinese Academy of Sciences (GIBHBRP24-02 to X.X.); the 111 Project (D18010 to J.Z.); the Natural Science Fund of Guangdong Province (2025A1515011245 to B.L.); the Young Doctoral Starting Sail Project of the Guangzhou Municipal Science and Technology Bureau (2024A04J4195 to B.L.). X.X. acknowledges Start-up grants from the Chinese Academy of Sciences.

Contributions

Q.Y., C.N., X.H., and B.L. conceived the study under the direction of X.X. and J.Z.; Q.Y. performed the initial antibody analysis and screening from the published data; C.N., B.L., X.H. and P.H. expressed and purified antibodies; B.L., C.N., and J.W. purified spikes and RBDs for cryo-EM and other experiments using constructs and protocols developed by X.X.; C.N., B.L., and L.W. performed BLI assays; X.H., H.Z., and Y.Y. performed pseudovirus and authentic virus neutralization assays; C.N. performed western blots to assay spike structural change; C.N., B.L., X.G., H.Y., and B.Z. preformed cryo-EM sample preparation and collected cryo-EM data under the supervision of J.H. and X.X.; X.G., C.N., and Z.L. processed cryo-EM data under the supervision of J.H. and X.X.; X.X., C.N., and B.L. analysed cryo-EM structures with assistance from X.G. and Q.Y.; Y.S., Q.Y., Y.Y., and F.W. performed AI-based antibody discovery under the supervision of J.Y.; C.N., Q.Y., B.L., X.G.

and X.H. prepared the figures under the supervision of X.X. and J.H.; X.X., C.N., and Q.Y. wrote the paper with input from all co-authors; G.H. and X.H. reviewed and edited the manuscript. X.X., Z.J., J.Y., J.H., L.C., and X.C. supervised the research.

Competing interests

The authors declare that they have no competing interests.

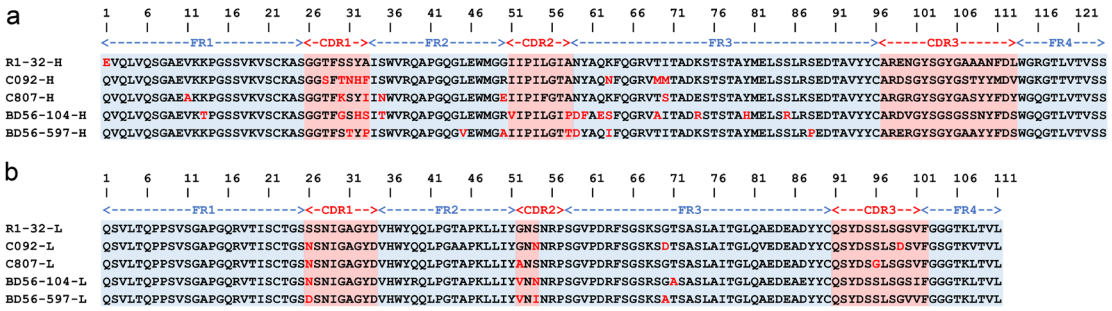

c

	WT	K417N	K417T	E484K	E484Q	T478K	L452R	L452Q	L452M	F490S	Alpha	Beta	Gamma	Kappa	Delta	Lambda
C092	0.046 (1.0)	0.093 (2.0)	0.019 (2.4)	0.042 (1.1)	0.048 (1.0)	0.058 (1.3)	0.072 (1.6)	0.200 (4.3)	0.040 (1.2)	0.128 (2.8)	0.050 (1.1)	0.093 (2.0)	0.096 (2.1)	0.127 (2.8)	0.179 (3.9)	0.436 (9.5)
C807	0.118 (1.0)	0.221 (1.9)	0.157 (1.3)	0.198 (1.7)	0.168 (1.4)	0.164 (1.4)	1.08 (9.2)	1.18 (10.0)	0.246 (2.1)	0.437 (3.7)	0.142 (1.2)	0.160 (1.4)	0.153 (1.3)	0.813 (6.9)	0.904 (7.7)	4.36 (36.9)
BD56-104	0.038 (1.0)	0.073 (1.9)	0.098 (2.6)	0.070 (1.8)	0.088 (2.3)	0.073 (1.9)	0.048 (1.3)	0.349 (9.2)	0.027 (1.4)	0.592 (15.6)	0.027 (1.4)	0.046 (1.2)	0.036 (1.1)	0.091 (2.4)	0.082 (2.2)	6.76 (178)
BD56-597	0.048 (1.0)	0.044 (1.1)	0.057 (1.2)	0.047 (1.0)	0.063 (1.3)	0.050 (1.0)	0.079 (1.6)	0.108 (2.3)	0.031 (1.5)	0.105 (2.2)	0.050 (1.0)	0.014 (3.4)	0.016 (3.0)	0.037 (1.3)	0.035 (1.4)	0.560 (11.7)
R1-32	0.931 (1.0)	1.13 (1.2)	N/A	3.55 (3.8)	2.96 (3.2)	2.12 (2.3)	54.2 (58.2)	34.9 (37.5)	N/A	11.8 (12.7)	0.709 (1.3)	10.3 (11.0)	N/A	92.1 (98.9)	72.6 (78.0)	953 (1023)

	BA.1	BA.1.1	BA.2	BA.3	BA.2.75	BA.2.75.2	BA.2.11	BA.2.12.1	BA.2.13	BA.4/5	BF.7	BQ.1.1	XBB	XBB.1.5	EG.5	EG.5.1
C092	0.142 (3.1)	0.016 (2.9)	0.022 (2.1)	0.032 (1.4)	0.017 (2.7)	0.085 (1.8)	0.032 (1.4)	0.213 (4.6)	0.022 (2.1)	0.132 (2.9)	0.293 (6.4)	0.200 (4.3)	0.056 (1.2)	0.073 (1.6)	0.056 (1.2)	0.059 (1.3)
C807	0.224 (1.9)	0.081 (1.5)	0.014 (8.4)	0.049 (2.4)	0.048 (2.5)	0.148 (1.3)	0.471 (4.0)	0.215 (1.8)	0.044 (2.7)	0.741 (6.3)	1.91(16.2)	2.01 (17.0)	0.194 (1.6)	0.640 (5.4)	0.653 (5.5)	0.677 (5.7)
BD56-104	0.122 (3.2)	0.024 (1.6)	0.021 (1.8)	0.031 (1.2)	0.099 (2.6)	0.167 (4.4)	0.049 (1.3)	0.087 (2.3)	0.020 (1.9)	0.029 (1.3)	0.598(15.7)	0.897 (23.6)	2.11 (55.5)	4.35 (114)	4.25 (112)	4.40 (116)
BD56-597	0.067 (1.4)	0.027 (1.8)	0.046 (1.0)	0.031 (1.5)	0.048 (1.0)	0.079 (1.6)	0.016 (3.0)	0.021 (2.3)	0.019 (2.5)	0.051 (1.1)	0.061 (1.3)	0.097 (2.0)	0.070 (1.5)	0.034 (1.4)	0.043 (1.1)	0.051 (1.1)
R1-32	1.13 (1.2)	N/A	N/A	N/A	N/A	N/A	N/A	N/A	N/A	55.5 (59.6)	129 (138)	212 (228)	49.2 (52.8)	N/A	N/A	N/A

Fold change relative to RBD-WT | affinity ≥ WT | Fold change < 10 | Fold change 10-100 | Fold change > 100

d

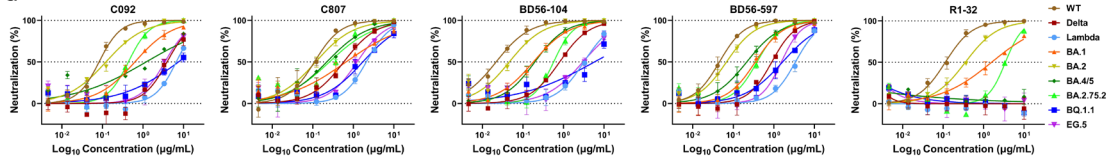

e

mAb	Pseudoviruses neutralization IC50 (μg/mL)								
	WT	Delta	Lambda	BA.1	BA.2	BA.4/5	BA.2.75.2	BQ.1.1	EG.5
C092	0.083	3.931	6.633	0.633	0.122	1.200	0.437	7.557	3.484
C807	0.110	0.582	2.095	0.665	0.118	0.222	0.259	1.717	1.245
BD56-104	0.022	0.807	3.211	0.181	0.046	0.197	0.574	5.844	3.026
BD56-597	0.046	0.896	3.427	0.350	0.068	0.216	0.387	1.654	1.542
R1-32	0.113	>10	>10	1.576	0.354	>10	3.465	>10	>10

f

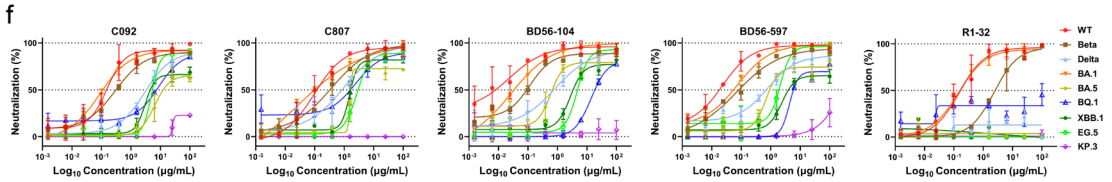

g

mAb	Authentic viruses neutralization IC50 (μg/mL)								
	WT	Beta	Delta	BA.1	BA.5	BQ.1	XBB.1	EG.5	KP.3
C092	0.151	0.293	2.878	0.085	6.329	8.575	3.042	5.004	>100
C807	0.094	0.356	0.944	0.021	1.578	2.401	1.517	2.671	>100
BD56-104	0.023	0.114	0.819	0.025	0.577	13.680	2.698	4.676	>100
BD56-597	0.023	0.067	0.765	0.073	0.693	4.310	2.376	2.099	>100
R1-32	0.151	2.343	>100	0.142	>100	>100	>100	>100	>100

Fig. 1. Sequence alignments, binding affinities, and neutralization activities of R1-32-like antibodies.

a-b, Heavy chain (**a**) and Light chain (**b**) sequence alignments of germline-like R1-32 with selected affinity-matured R1-32-like antibodies (C092, C807, BD56-104, BD56-597). The sequences of R1-32 are used as the references, with somatic hypermutation-derived amino

1156 acids marked in red. The HCDRs and LCDRs residues are highlighted in salmon. **c**, Binding
1157 affinities of R1-32-like antibodies to a panel of SARS-CoV-2 RBDs. Binding assays were
1158 performed using biolayer interferometry (BLI). Dissociation constant K_Ds (nM) are shown,
1159 with fold changes relative to wild-type RBD indicated in parentheses. RBDs carrying L452,
1160 F490, or both substitutions are colored in red, blue, and purple, respectively. Binding
1161 affinities higher than the wild-type RBD are shown in blue, whereas reduced affinities (<10-
1162 fold, 10-100-fold, and >100-fold relative to wild-type) are shown in green, yellow, and
1163 orange, respectively. For R1-32, the K_Ds of Alpha, Beta, BA.1, K417N, E484K/Q, T478K,
1164 and L452Q were obtained from our previously published work [27]. N/A means untested. RBD
1165 binding curves are shown in **Fig. 4f and Fig. S1b-e,** and K_D data used for comparisons are
1166 shown in **Tables S1 and S4**. **d**, Neutralization activities of R1-32-like antibodies towards
1167 SARS-CoV-2 wild-type, Delta, Lambda, Omicron BA.1, BA.2, BA.4/5, BA.2.75.2, and
1168 BQ.1.1 pseudoviruses. Data are presented as mean ± SD (n = 2). IC_{50} values are summarized
1169 in **e**. **f**, Neutralization activities of R1-32-like antibodies towards WT, Beta, Delta, Omicron
1170 BA.1, BA.5, BQ.1, XBB.1, EG.5, and KP.3 authentic viruses. Data are presented as mean ±
1171 SD (n = 2). IC_{50} values are summarized in **g.**

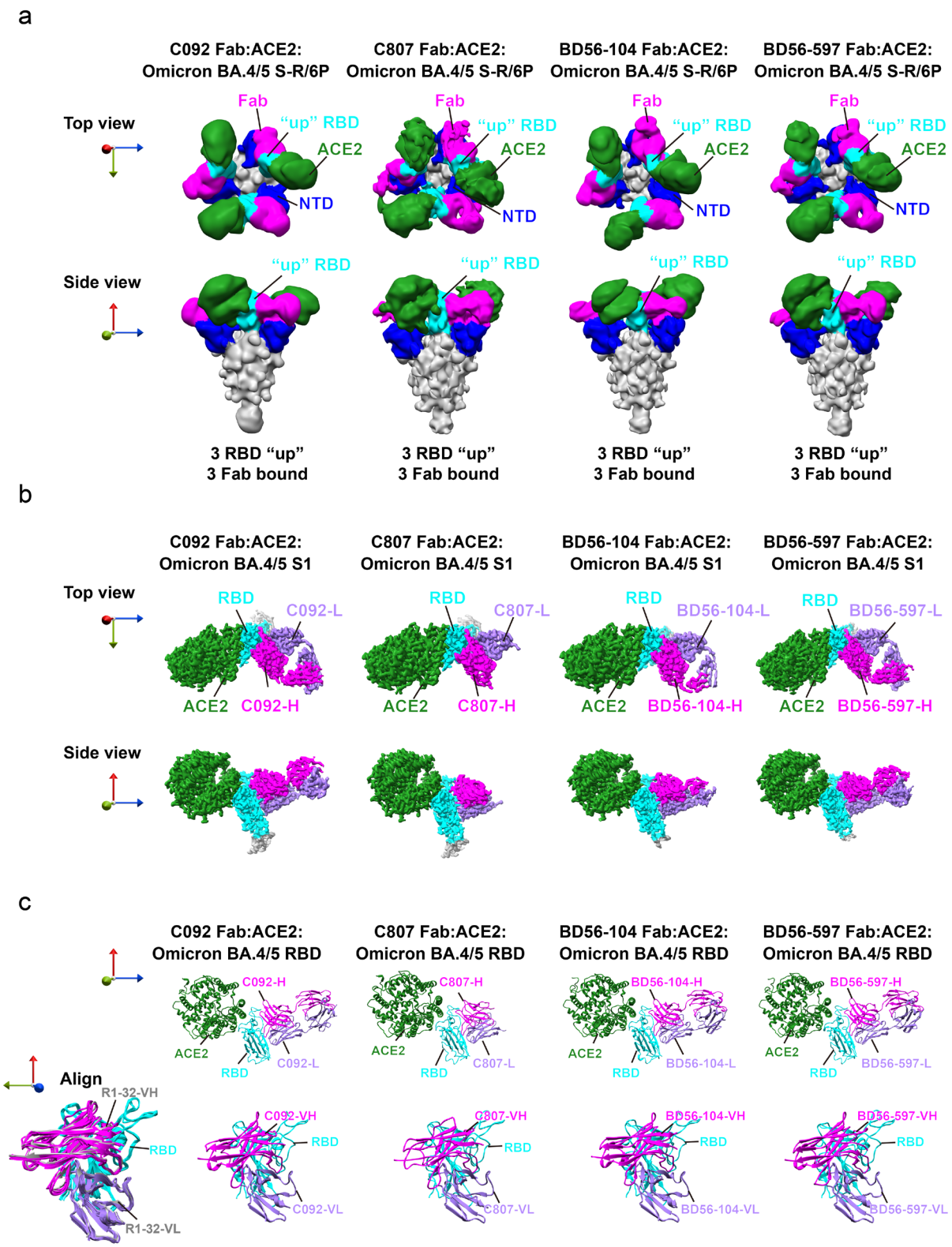

Fig. 2. Structures of mutation-tolerant antibodies in complex with SARS-CoV-2 BA.4/5 S-trimer and ACE2.

a, Cryo-EM densities (low-pass filtered to 12 Å) of BA.4/5 S-R/6P S-trimer bound to Fab and ACE2 at 3:3:3 molar ratio. C092, C807, BD56-104, and BD56-597 Fabs, NTD, RBD, and ACE2 are colored in magenta, blue, cyan, and dark green, respectively; the rest of the S-

trimer is colored in grey. The 3 RBDs in “up” positions are indicated, each simultaneously engaging both ACE2 and antibody. **b**, Cryo-EM densities of BA.4/5 S1 bound to Fab and ACE2. C092, C807, BD56-104, and BD56-597 Fab-HC, Fab-LC, NTD, RBD, and ACE2 are colored in magenta, purple, blue, cyan, and dark green, respectively; the rest of the S1 is colored in grey. **c**, Structures of the BA.4/5 RBD:Fab:ACE2 complex (**upper panels**) derived from the density shown in panel **b**. Individual binding modes of C092, C807, BD56-104, and BD56-597 to the RBD are shown in the lower panels. Superposition of C092, C807, BD56-104, BD56-597, and R1-32 bound to RBD is shown in the left panels, with C092, C807, BD56-104, and BD56-597 Fabs rendered in color and the R1-32 Fab shown in grey.

a

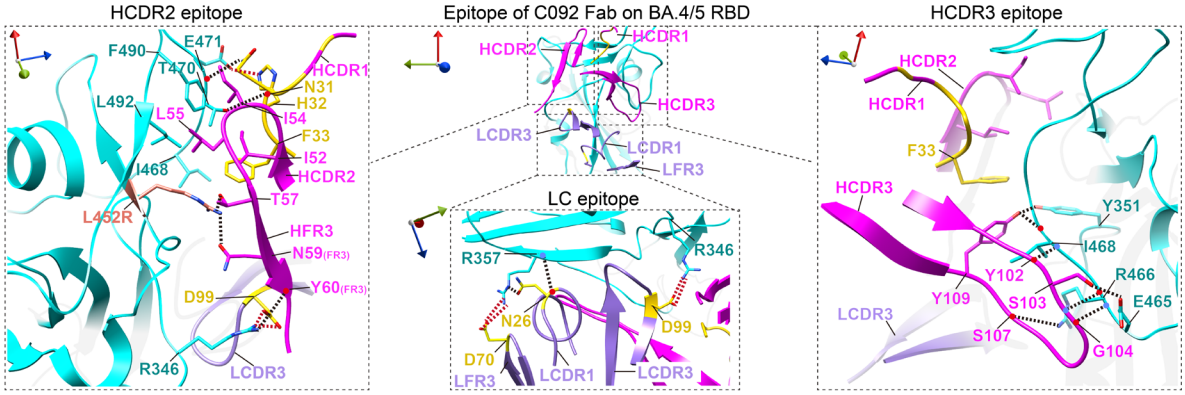
HCDR2 epitope
Epitope of C092 Fab on BA.4/5 RBD
HCDR3 epitope
LC epitope
F490
E471
T470
HCDR1
N31
H32
L492
L55
I54
F33
I52
HCDR2
I468
T57
L452R
HFR3
N59(FR3)
Y60(FR3)
D99
R346
LCDR3
HCDR2
HCDR1
HCDR3
LCDR3
LCDR1
LFR3
R357
R346
N26
D99
D70
LFR3
LCDR1
LCDR3
HCDR2
HCDR1
F33
HCDR3
Y351
I468
Y102
R466
Y109
S103
E465
LCDR3
S107
G104

b

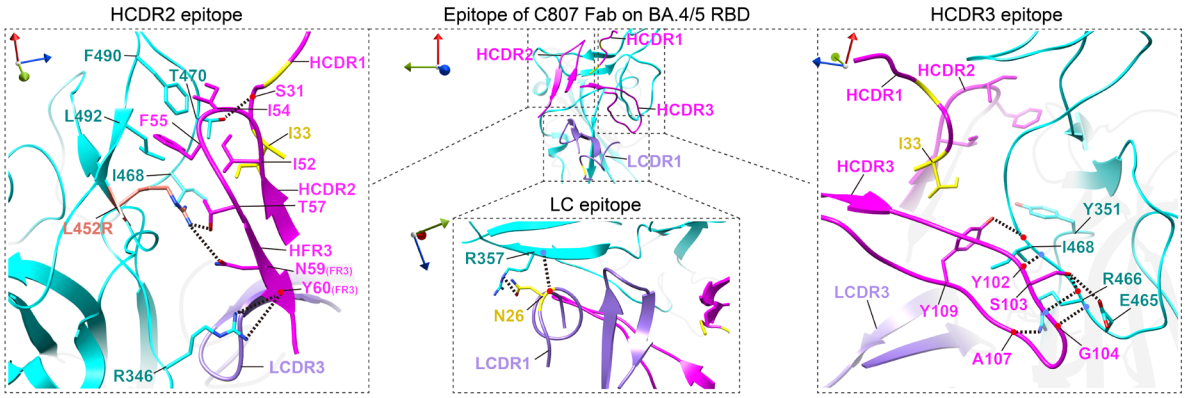
HCDR2 epitope
Epitope of C807 Fab on BA.4/5 RBD
HCDR3 epitope
LC epitope
F490
T470
HCDR1
S31
L492
F55
I54
I33
I52
I468
HCDR2
T57
L452R
HFR3
N59(FR3)
Y60(FR3)
R346
LCDR3
HCDR2
HCDR1
HCDR3
LCDR1
R357
N26
LCDR1
HCDR2
HCDR1
I33
HCDR3
Y351
I468
Y102
R466
LCDR3
Y109
S103
E465
A107
G104

c

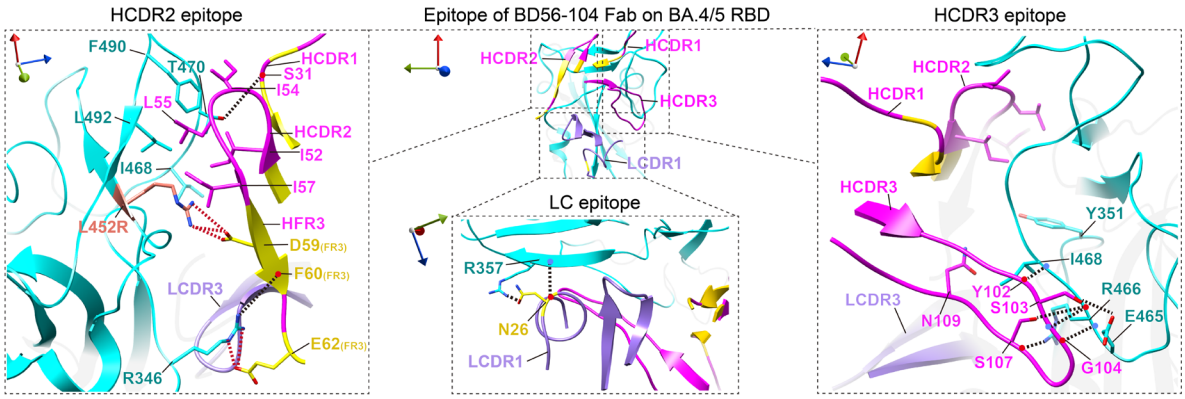
HCDR2 epitope
Epitope of BD56-104 Fab on BA.4/5 RBD
HCDR3 epitope
LC epitope
F490
T470
HCDR1
S31
I54
L55
L492
HCDR2
I52
I468
I57
L452R
HFR3
D59(FR3)
F60(FR3)
LCDR3
E62(FR3)
R346
HCDR2
HCDR1
HCDR3
LCDR1
R357
N26
LCDR1
HCDR2
HCDR1
HCDR3
Y351
I468
Y102
R466
LCDR3
N109
S103
E465
S107
G104

d

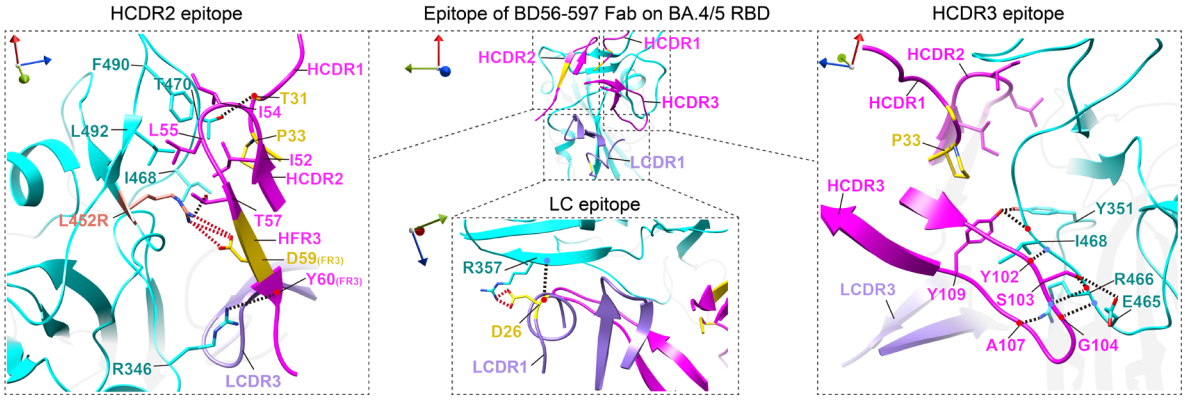
HCDR2 epitope
Epitope of BD56-597 Fab on BA.4/5 RBD
HCDR3 epitope
LC epitope
F490
T470
HCDR1
T31
I54
L492
L55
P33
I52
I468
HCDR2
L452R
T57
HFR3
D59(FR3)
Y60(FR3)
R346
LCDR3
HCDR2
HCDR1
HCDR3
LCDR1
R357
D26
LCDR1
HCDR2
HCDR1
P33
HCDR3
Y351
I468
Y102
R466
LCDR3
Y109
S103
E465
A107
G104

1188 **Fig. 3. Epitopes of mutation-tolerant antibodies on BA.4/5 RBD.**

1189 **a-d**, HCDR2, HCDR3, and LC epitopes of C092 (**a**), C807 (**b**), BD56-104 (**c**), BD56-597 (**d**)
1190 are shown from rotated views. RBD, Fab-HC, and Fab-LC residues are colored in cyan,
1191 magenta, and purple, respectively. Antibody residues introduced by somatic hypermutation
1192 are colored in yellow, while residue L452R mutated in BA.4/5 RBD is colored in salmon.
1193 The backbone carbonyl oxygens and amide nitrogens are indicated by red and blue dots,
1194 respectively. Hydrogen bonds and salt bridges are shown as black and red dash lines,
1195 respectively.

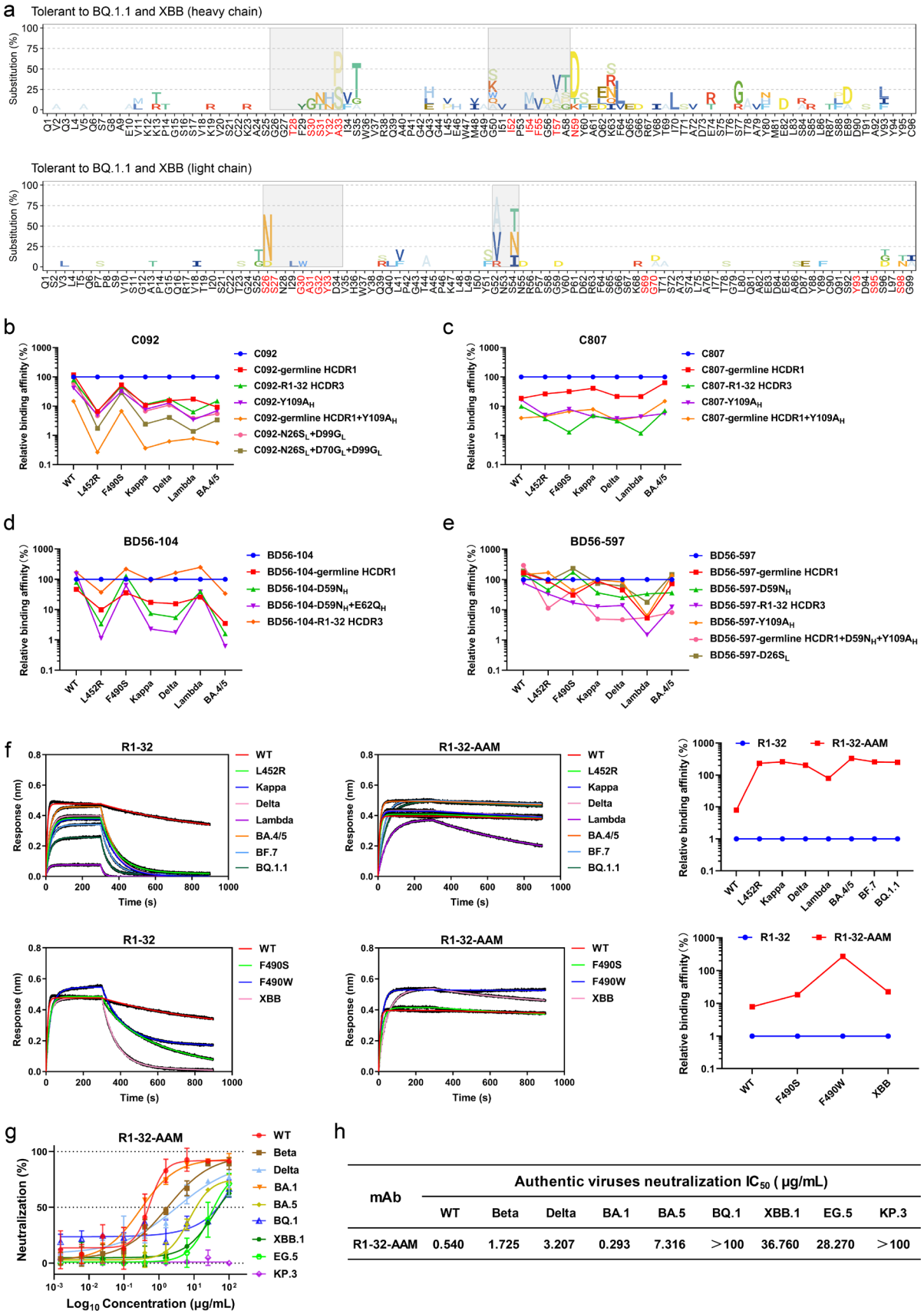

h

mAb	Authentic viruses neutralization IC_{50} (μg/mL)								
	WT	Beta	Delta	BA.1	BA.5	BQ.1	XBB.1	EG.5	KP.3
R1-32-AAM	0.540	1.725	3.207	0.293	7.316	>100	36.760	28.270	>100

1196

1197 **Fig. 4. Affinity maturation confers mutation tolerance to R1-32-like**
1198 **antibodies.**

1199 **a,** Frequency of somatic hypermutations (SHMs) in R1-32-like antibodies tolerant to BQ.1.1
1200 and XBB. The residues involved in epitope binding are colored in red. **b-e**, Relative binding
1201 affinities of antibody mutants derived from C092 (**b**), C807 (**c**), BD56-104 (**d**), and BD56-
1202 597 (**e**) to the RBDs of SARS-CoV-2 wild-type, L452R, F490S, Kappa, Delta, Lambda, and
1203 BA.4/5. The constructed C092 mutants include C092-germline HCDR1 (HCDR1 reverted to
1204 germline sequence), C092-R1-32 HCDR3 (HCDR3 replaced with R1-32 HCDR3), C092-
1205 Y109A_H, C092-germline HCDR1+Y109A_H, C092-N26S_L+D99G_L, and C092-
1206 N26S_L+D70G_L+99G_L. The C807 mutants include C807-germline HCDR1, C807-R1-32
1207 HCDR3, C807-Y109A_H, and C807-germline HCDR1+Y109A_H. The BD56-104 mutants
1208 include BD56-104 germline HCDR1, BD56-104-D59N_H, BD56-104+D59N_H+E62Q_H, and
1209 BD56-104-R1-32 HCDR3. The BD56-597 mutants include BD56-597-germline HCDR1,
1210 BD56-597-D59N_H, BD56-597-R1-32 HCDR3, BD56-597-Y109A_H, BD56-597-germline
1211 HCDR1-D59N_H+Y109A_H, BD56-597-D26S_L. Affinity changes of mutants are normalized to
1212 K_Ds of the corresponding unmodified antibody (set as 100%). Binding curves are shown in
1213 **Fig. S11a-d,** and K_D values used for comparisons are shown in **Table S3**. **f**, Binding curves
1214 of R1-32 and R1-32-AAM to the RBDs of wild-type, L452R, Kappa, Delta, Lambda, BA.4/5,
1215 BF.7, BQ.1.1, F490S, F490W, and XBB. Affinity changes of R1-32-AAM are normalized to
1216 K_Ds of R1-32 (set as 1%). K_D values used for comparisons are shown in **Table S4**. **g**,
1217 Neutralization activities of R1-32-AAM towards SARS-CoV-2 wild-type, Beta, Delta,
1218 Omicron BA.1, BA.5, BQ.1, XBB.1, EG.5, and KP.3 authentic viruses. Data are presented as
1219 mean ± SD (n = 2). IC_{50} values are summarized in **h**.

a

	type-1									type-2	type-3		
	SARS-CoV-2	Pangolin-CoV -GD-2019	Bat-CoV-RaTG13	Pangolin-CoV -GX-2017	Laos-20-52	Laos-20-236	Bat-CoV-RsSHC014	Bat-CoV-WIV1	SARS-CoV-1	BtKY72	GX2013	HeB2013	RmYN02
C092	0.046	0.111	0.177	0.262	0.059	0.034	0.622	21.3	no binding	29.2	26.3	34.9	31.5
C807	0.118	0.613	0.738	0.469	0.972	0.687	3.50	7.50	341	54.5	31.1	103	20.3
BD56-104	0.038	0.177	0.227	0.117	0.144	0.082	48.0	no binding	no binding	weak binding	weak binding	weak binding	weak binding
BD56-597	0.048	0.016	0.284	0.086	0.104	0.033	0.198	7.19	weak binding	223	159	weak binding	287
ZL525	0.295	0.040	0.020	0.104	0.362	0.810	0.447	7.54	63.1	18.0	3.89	14.1	2.63
R1-32	0.931	0.777	38.2	4.76	0.963	1.80	297	no binding	no binding	no binding	no binding	no binding	no binding

K_D (nM) < 1 | 1-100 | > 100 | no binding

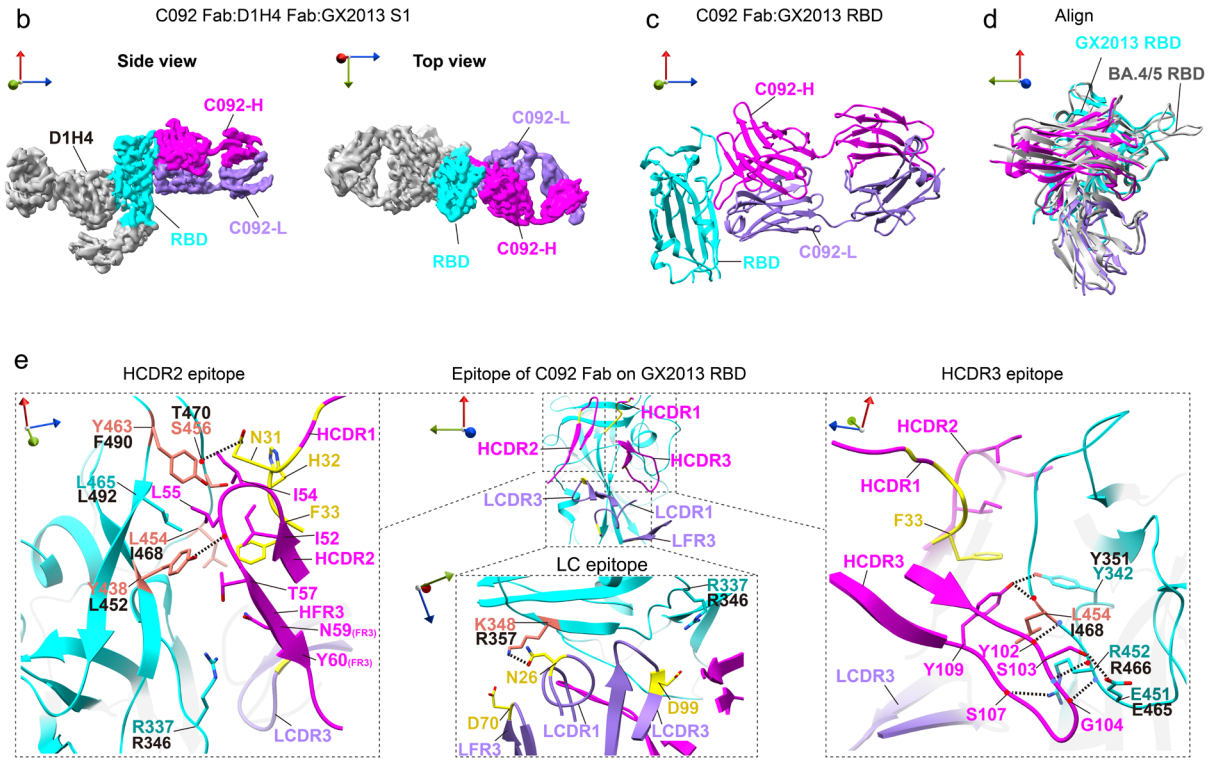

Fig. 5. Affinity maturation confers R1-32-like antibodies with broader SARSr-CoVs binding.

a, Binding affinities of R1-32-like antibodies to the RBDs of SARS-related coronaviruses (SARSr-CoVs). K_Ds (nM) are shown, with values <1, 1-100, >100 nM, and no binding colored in green, yellow, orange, and red, respectively. Binding curves and detailed kinetic parameters are provided in **Fig. S12 and Table S5**. **b**, Cryo-EM densities of the GX2013 S1:C092 Fab:D1H4 Fab complex. C092 Fab-HC, Fab-LC, and RBD are colored in magenta, purple, and cyan, respectively; the rest of the S1 and D1H4 Fab are colored grey. **c**, Structure of the GX2013 RBD:C092 Fab complex derived from the density in panel **b**. **d**, Comparison of C092 binding to GX2013 RBD and BA.4/5 RBD; the BA.4/5 RBD:C092 Fab complex is shown in grey. **e**, C092 HCDR2, HCDR3, and LC epitopes are shown from rotated views. Residues introduced by somatic hypermutation are colored in yellow, and epitope residues differing from SARS-CoV-2 wild-type RBD are colored in salmon. GX2013 RBD residues are labeled with the corresponding SARS-CoV-2 residues indicated in black. The backbone

carbonyl oxygens and amide nitrogens are indicated by red and blue dots, respectively, and hydrogen bonds are shown as black dash lines.

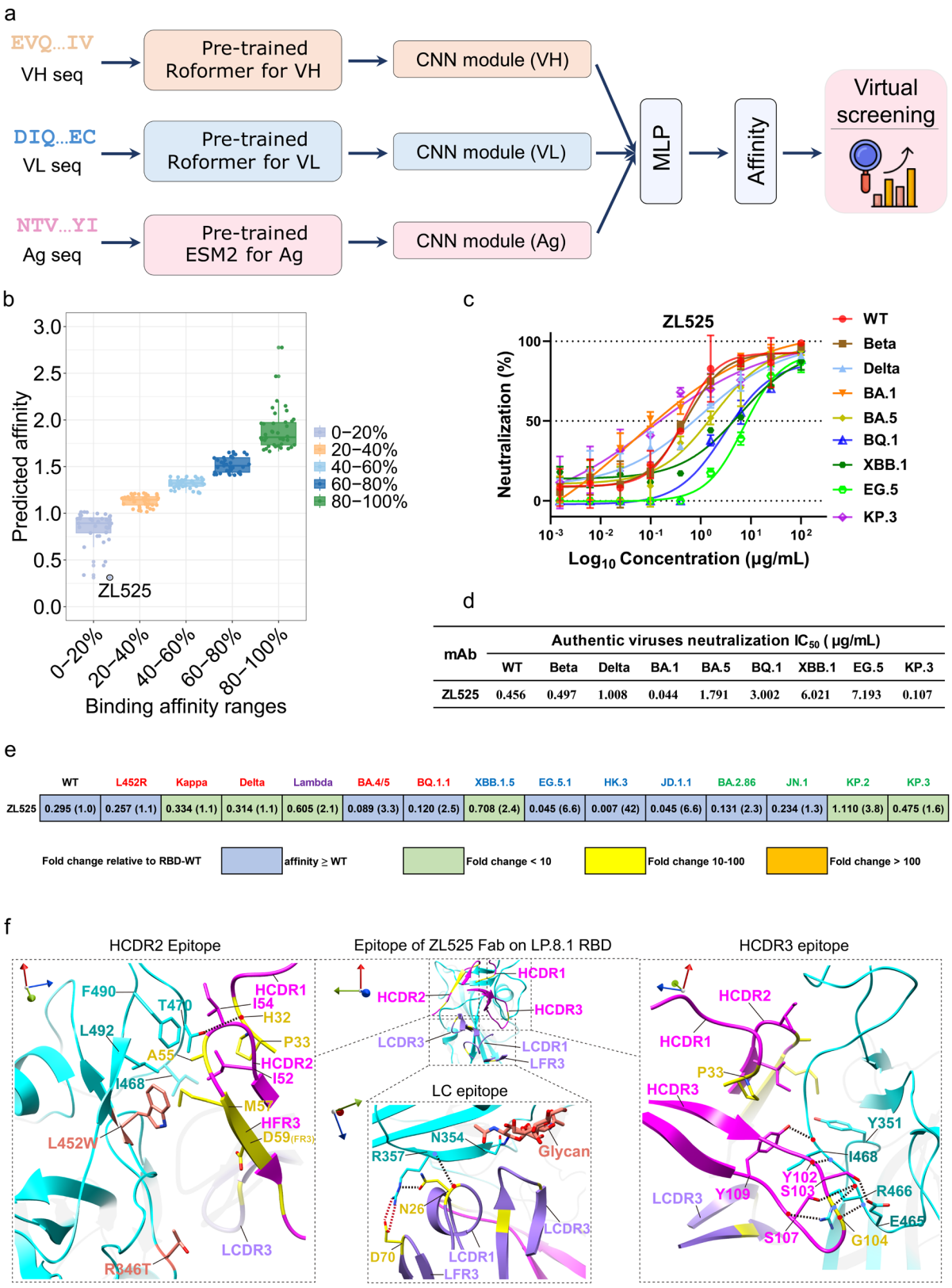

Fig. 6. AI-guided discovery and structural characterization of the glycan-tolerant broadly neutralizing antibody ZL525.

a, Workflow of the virtual screening pipeline based on pre-trained antibody language models. **b**, Distribution of predicted affinities of the 190 R1-32-like mAbs. **c**, Neutralization activities

of the ZL525 towards SARS-CoV-2 wild-type, Beta, Delta, Omicron BA.1, BA.5, BQ.1, XBB.1, EG.5, and KP.3 authentic viruses. Data are shown as mean ± SD (n = 2). IC_{50} values are summarized in **d**. **e,** Binding affinities of ZL525 to RBDs carrying $L452_{SARS2}$ or $F490_{SARS2}$ substitutions and newly emerging variants. Dissociation constant K_Ds (nM) are shown, with fold changes relative to wild-type RBD indicated in parentheses. Binding affinities higher than the wild-type RBD are shown in blue, whereas reduced affinities (<10-fold, 10-100-fold, and >100-fold relative to wild-type) are shown in green, yellow, and orange, respectively. RBDs carrying L452, F490, or both substitutions are colored in red, blue, and purple, respectively. RBDs carrying L452 substitution together with N354 glycosylation are colored in green. Binding assays were performed by BLI, and detailed kinetic parameters are provided in **Table S8. f**, ZL525 HCDR2, HCDR3, and LC epitopes are shown from rotated views. Antibody residues introduced by somatic hypermutation are colored in yellow, and residues $L452W_{SARS2}$ and $R346T_{SARS2}$ mutated in the LP.8.1 RBD are colored in salmon. The backbone carbonyl oxygens and amide nitrogens are indicated by red and blue dots, respectively. Hydrogen bonds and salt bridges are shown as black and red dash lines, respectively.